Observation of Wave-Packet Branching through an Engineered Conical Intersection

Christopher S. Wang, ^{1,2,*} Nicholas E. Frattini, ^{1,2} Benjamin J. Chapman, ^{1,2} Shruti Puri, ^{1,2} S. M. Girvin, ^{1,2} Michel H. Devoret, ^{1,2} and Robert J. Schoelkopf, ^{1,2,†}

¹Departments of Physics and Applied Physics, Yale University, New Haven, Connecticut 06511, USA

²Yale Quantum Institute, Yale University, New Haven, Connecticut 06520, USA

(Received 16 May 2022; revised 1 November 2022; accepted 19 December 2022; published 26 January 2023)

Analog quantum simulators, which efficiently represent model systems, have the potential to provide new insight toward naturally occurring phenomena beyond the capabilities of classical computers. Incorporating dissipation as a resource unlocks a wider range of out-of-equilibrium processes such as chemical reactions. Here, we operate a hybrid qubit-oscillator circuit quantum electrodynamics simulator and model nonadiabatic molecular dynamics through a conical intersection. We identify dephasing of the electronic qubit as the mechanism that drives wave-packet branching when the corresponding oscillator undergoes large amplitude motion. Furthermore, we directly observe enhanced branching when the wave-packet passes through the conical intersection. Thus, the forces that influence a chemical reaction can be viewed from the perspective of measurement backaction in quantum mechanics—there is an effective measurement-induced dephasing rate that depends on the position of the wave packet relative to the conical intersection. Our results set the groundwork for more complex simulations of chemical dynamics using quantum simulators, offering deeper insight into the role of dissipation in determining macroscopic quantities of interest such as the quantum yield of a chemical reaction.

DOI: 10.1103/PhysRevX.13.011008 Subject Areas: Quantum Physics

I. INTRODUCTION

Quantum processors applied to quantum chemistry have mostly focused on calculating static electronic energies [1], though experimental demonstrations have been limited to variational methods in the current near term intermediatescale quantum era of devices [2,3]. Modeling molecular dynamics that ensue from interaction with light, however, is a driven-dissipative many-body problem that goes beyond just calculating the fermionic electronics and includes the dynamics of bosonic rotational and vibrational degrees of freedom as well. Electronic transport dynamics have been investigated using quantum processors in the context of light harvesting in photosynthesis, where individual sites are approximated as two-level systems and encoded in qubits [4,5]. Vibrational dynamics and vibronic spectra have also been simulated using bosonic modes that can support multiphoton states [6–8], but only under the adiabatic Born-Oppenheimer approximation.

Published by the American Physical Society under the terms of the Creative Commons Attribution 4.0 International license. Further distribution of this work must maintain attribution to the author(s) and the published article's title, journal citation, and DOI. In many polyatomic molecules, nonadiabatic couplings between potential energy surfaces influence a wide range of photoinduced chemical processes [9]. Central to nonadiabatic dynamics are features known as conical intersections (CIs), which indicate an electronic degeneracy that invalidates the Born-Oppenheimer approximation and results in strong hybridization between the electronic and nuclear degrees of freedom. This hybridization has immense consequences for excited state dynamics when the molecular wave packet traverses these intersections, producing, for example, ultrafast radiationless reactions. Using quantum simulators to study nonadiabatic dynamics has been proposed with digital quantum computers [10] and trapped-ion systems [11–13], but experimental demonstrations have remained elusive.

In this work, we experimentally demonstrate dissipative nonadiabatic dynamics using a circuit quantum electrodynamics (circuit QED) quantum simulator. Using microwave drives, we engineer a CI in a system containing one qubit and two harmonic oscillators. The qubit represents two electronic energy levels that are modulated by two generalized nuclear coordinates encoded in harmonic oscillators. Our approach uses a simple and optimal one-to-one mapping of the three modes of the model to three modes of our simulator; this native mapping enables the approach's hardware efficiency and can be straightforwardly scaled up using existing multimode systems [14,15]. Importantly, we engineer intrinsic qubit coherence times an order of magnitude longer than the timescale of the

^{*}Corresponding author. christopher.wang@yale.edu †Corresponding author. robert.schoelkopf@yale.edu

engineered dissipation. This corresponds to the physical scenario where the dynamics are not dominated by spontaneous emission of the electronic excitation. By simultaneously measuring the qubit and performing Wigner tomography [16] of one of the oscillators as they evolve under a control Hamiltonian, we correlate qubit dephasing events with wave-packet branching. Finally, when the CI is active, we observe enhanced branching when the wave packet passes through the CI. This can be understood as a competition between the measurement-induced dephasing strength and a position-dependent electronic energy gap. Our results demonstrate that superconducting circuits possess all of the capabilities required to implement faithful simulations of nonadiabatic dynamics.

II. MODEL CONICAL INTERSECTION HAMILTONIAN

The variety of numerical methods and associated models developed for addressing nonadiabatic molecular dynamics on classical computers is vast [17–19]. Common to all of these methods are various approximations which reduce the computational cost compared to exact solutions, which of course scale exponentially with system size. For quantum simulation of nonadiabatic problems, we seek models that treat all degrees of freedom quantum mechanically; this

effectively translates to a basis choice. Vibronic coupling (VC) model Hamiltonians [20] use a diabatic basis for the electronic eigenfunctions in order to avoid divergence issues associated with the standard adiabatic basis in the vicinity of a CI [21]. See Appendix A for a more detailed discussion of the choice of basis. VC Hamiltonian parameters may be either empirically fit to reproduce experimental data [22] or obtained from *ab initio* calculations such as for pyrazine [23] and pyrene [24]. Computational studies investigating the influence of various forms of rovibrational damping on nonadiabatic dynamics utilize VC Hamiltonians with different approximations for the bath [25–27].

In this work, we consider a linear vibronic coupling (LVC) model—the simplest VC Hamiltonian that contains a conical intersection—with two electronic states $\{|+\rangle, |-\rangle\}$ coupled to two generalized rovibrational modes \hat{a} and \hat{b} :

$$\hat{H}_a/\hbar = \Delta_a \hat{a}^{\dagger} \hat{a} + \underbrace{g_x \hat{\sigma}_x (\hat{a} + \hat{a}^{\dagger})}_{\hat{g}_a}, \tag{1}$$

$$\hat{H}_b/\hbar = \Delta_b \hat{b}^{\dagger} \hat{b} + \underbrace{g_y \hat{\sigma}_y (\hat{b} + \hat{b}^{\dagger})}_{\hat{b}_b}, \tag{2}$$

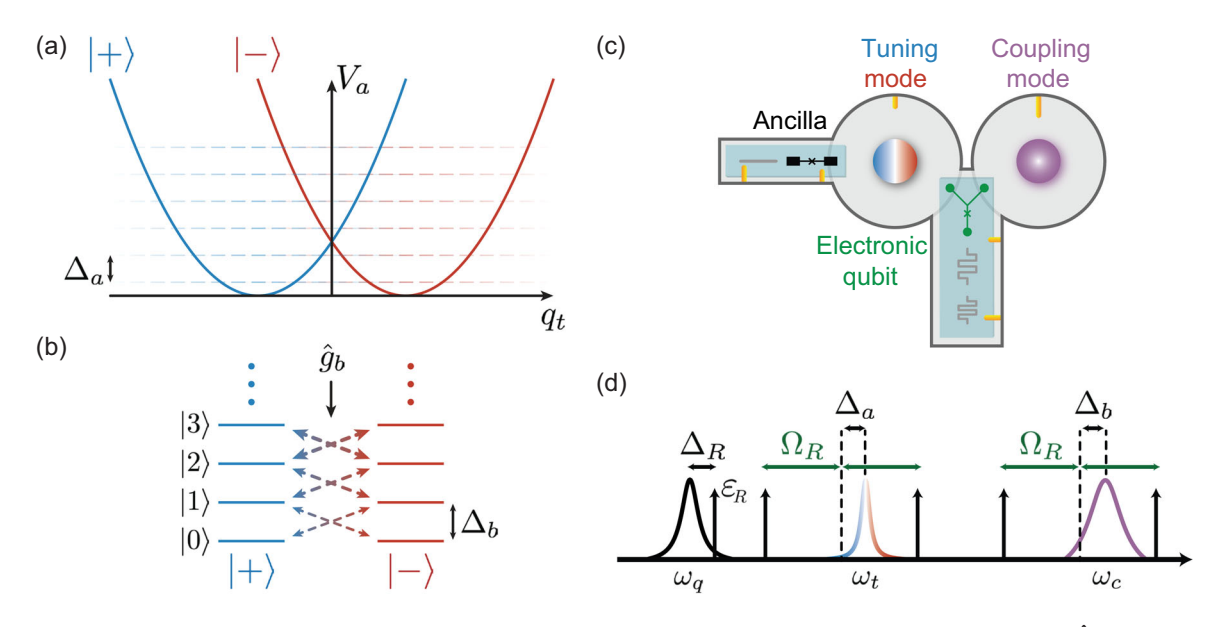


FIG. 1. Model molecular Hamiltonian with a conical intersection and experimental setup. (a) Eigenspectrum of \hat{H}_a , which consists of two displaced quantum harmonic oscillator Fock ladders (dashed lines) of the tuning mode depending on if the qubit is in $|+\rangle$ (blue) or $|-\rangle$ (red). (b) In the basis of $|\pm\rangle$ for the qubit, the addition of $\hat{g}_b = g_y \hat{\sigma}_y (\hat{b} + \hat{b}^{\dagger})$ on top of \hat{H}_a couples the two Fock ladders of the coupling mode (with energy $\Delta_b \hat{b}^{\dagger} \hat{b}$) via $\hat{\sigma}_y = |+\rangle \langle -|+|-\rangle \langle +|$ (dashed arrows) for each Fock state of the tuning mode. Hence, dynamics of the coupling mode can cause transitions between $|\pm\rangle$. (c) Schematic of the circuit QED device used in this experiment. The tuning and coupling modes are 3D $\lambda/4$ coaxial resonators which are coupled to an electronic qubit (encoded in a transmon) with a readout resonator and Purcell filter [31]. An additional ancilla module with a transmon mode and readout resonator is coupled to the tuning mode for independent state tomography. The coupling mode is intentionally overcoupled to a 50 Ω transmission line, resulting in a linewidth $\kappa_b/2\pi \approx 320$ kHz. (d) Relative mode frequencies and drive configuration used to enact $\hat{H}_{\rm LVC}$. A full table of system parameters is given in Appendix C.

$$\hat{H}_{LVC} = \hat{H}_a + \hat{H}_b, \tag{3}$$

where our electronic states $|\pm\rangle$ are eigenstates of $\hat{\sigma}_r$. Our model contains first-order intrastate and interstate coupling strengths g_x and g_y , respectively, as well as generalized rovibrational frequencies Δ_a and Δ_b . We refer to modes \hat{a} and \hat{b} as tuning and coupling modes, respectively, as the dimensionless coordinate $\hat{q}_t = \hat{a} + \hat{a}^{\dagger}$ "tunes" the energy between the electronic states $|\pm\rangle$ and $\hat{q}_c = \hat{b} + \hat{b}^{\dagger}$ mediates coupling between the two electronic states via $\hat{\sigma}_v =$ $|+\rangle\langle -|+|-\rangle\langle +|$ (see Appendix A for a detailed conversion to conventional position and momentum operators). We identify the position \hat{q}_t of the tuning mode as a reactive coordinate, which typically undergoes large amplitude motion for real systems of interest. It is important to emphasize, however, the generalized nature of these coordinates in the diabatic basis; one will need to perform a diabatic-to-adiabatic transformation for extracting adiabatic populations [28].

The eigenstates of \hat{H}_a are depicted in Fig. 1(a). The electronic states and tuning mode are coupled by a conditional displacement interaction that shifts the equilibrium position of the oscillator depending on the electronic state. In the absence of any operator that couples $|+\rangle$ and $|-\rangle$, an initial state $|\psi\rangle = |\pm\rangle \otimes |\psi_0\rangle_a$, where $|\psi_0\rangle_a$ is an arbitrary state of the tuning mode, will evolve along the corresponding harmonic potential with the qubit remaining in $|\pm\rangle$. The addition of \hat{g}_b couples the electronic states via the states of the coupling mode, as shown in Fig. 1(b). The combination of \hat{g}_a and \hat{g}_b defines the conical intersection [29]. The full eigenspectrum of \hat{H}_{LVC} is not easily depicted, as it involves entangled states in the uncoupled basis of all three modes. We note that our description of the tuning and coupling modes would be interchanged had we elected to focus on the eigenstates of $\hat{\sigma}_{v}$. This model has historical origins in the well-known Jahn-Teller effect which was originally thought to be rooted in molecular symmetries. More recently, though, the model has been extended to larger polyatomic molecules with CIs that are not necessarily symmetry induced [30].

III. EXPERIMENTAL IMPLEMENTATION

In this work, we operate a quantum simulator realized as a 3D circuit QED processor [8] where the nuclear tuning and coupling modes are represented by $\lambda/4$ coaxial cavity modes and the electronic degree of freedom is encoded in a transmon qubit [32] [Fig. 1(c)]. The tuning mode is long-lived with a linewidth $\kappa_a/2\pi \approx 0.23$ kHz, whereas the coupling mode is overcoupled to a 50 Ω transmission line, resulting in a decay rate $\kappa_b/2\pi \approx 320$ kHz. We engineer $\hat{H}_{\rm LVC}$ [Eq. (3)] in a driven, rotating frame by combining a strong Rabi drive on the transmon, which results in an effective dressed qubit with an energy splitting of Ω_R , with simultaneous red and blue sideband drives on the cavity

modes detuned by $\mp\Omega_R$ [Fig. 1(d)]. This technique has been previously developed to simultaneously measure noncommuting qubit observables [33], foreshadowing the intimate link between measurement and the dissipative dynamics of our model system. Our desire to control multiphoton wave packets in the tuning mode requires a larger Rabi frequency than used previously [33]. This is needed to maintain the validity of the rotating wave approximation (RWA). To this end, we incorporate a static detuning Δ_R on the Rabi drive and adiabatically prepare the driven qubit eigenstates. This enables large Rabi frequencies while suppressing leakage to higher levels of the driven transmon (see Appendix B).

A. Simulator calibrations

A key requirement of our quantum simulator is the ability to initialize and perform tomography of the electronic qubit, which in our experiment is encoded by a driven transmon with an effective Rabi frequency Ω_R that is defined by the amplitude ε_R and static detuning Δ_R of the Rabi drive. In the frame of a single Rabi drive on the transmon, the driven Hamiltonian has the form $\hat{H}_d = (\Omega_R/2)\hat{\sigma}_z$ where $\hat{\sigma}_z =$ $|\tilde{g}\rangle\langle\tilde{g}|-|\tilde{e}\rangle\langle\tilde{e}|$ when expressed in the driven eigenbasis spanned by $\{|\tilde{g}\rangle, |\tilde{e}\rangle\}$ that adiabatically connects to the undriven transmon eigenstates $\{|g\rangle, |e\rangle\}$. We note that $|\tilde{g}\rangle \approx$ $(1/\sqrt{2})(|g\rangle + |e\rangle)$ and $|\tilde{e}\rangle \approx (1/\sqrt{2})(|g\rangle - |e\rangle)$, with minor contributions from higher excited states, when expressed in the basis of undriven transmon eigenstates. The conditional displacement interactions that we engineer in our experiment $\{\hat{H}_a, \hat{H}_b\}$ are conditioned on Pauli operators whose eigenstates lie on the equator of the *driven* Bloch sphere (i.e., $\hat{\sigma}_x$ and $\hat{\sigma}_{v}$), and thus will precess around the equator at a rate Ω_{R} . We can use this high frequency precession as a way of precisely calibrating Ω_R , which in turn lets us measure the expectation value of any Pauli operator aligned on the equator of the driven Bloch sphere over time. As long as the Rabi frequency is constant as a function of time, this technique is compatible with any interaction Hamiltonian that involves our driven qubit including \hat{H}_a , \hat{H}_b , and \hat{H}_{LVC} . For the free evolution case where only the Rabi drive is on and no cavity sidebands are active, we measure $\langle \hat{\sigma}_{x} \rangle$ as a function of time and extract a corresponding driven coherence time $T_{2\rho} = 27 \,\mu s$ [34]. This further elucidates the reasoning behind our chosen convention for the Pauli operators in Eqs. (1) and (2); we prefer the eigenstates of $\hat{\sigma}_z$ to be stationary in the frame of the drive. Full details of this measurement scheme are described in Appendix D.

The goal of our experiment is to understand the dynamics of the subsystem consisting of the electronic qubit and tuning mode under the influence of the conical intersection and dissipation in the coupling mode. The symmetry between the two interactions \hat{H}_a and \hat{H}_b is broken by their disparate dissipation rates, which results in qualitatively different dynamics. Specifically, we work in the

coherent regime where $g_x \gg \kappa_a$ for the tuning mode and the dissipative regime $g_y \lesssim \kappa_b$ for the coupling mode. As such, we proceed to calibrate and characterize each interaction independently before combining them together to study the full Hamiltonian \hat{H}_{LVC} of interest that includes the conical intersection.

We first calibrate the conditional displacement interaction \hat{H}_a on the tuning mode, which determines how coherent wave packets in the tuning mode propagate for each electronic state in the absence of the coupling mode. For clarity, we will describe coherent wave packets in the tuning mode as reactive wave packets following our earlier designation that the position of the tuning mode is a reactive coordinate of interest in a molecular system that undergoes large amplitude motion. This Hamiltonian produces two distinct harmonic potential energy surfaces whose equilibrium positions are offset from the origin by an amount $\pm \alpha_g$, where $\alpha_g = g_x/\Delta_a$ for each electronic state $|\mp\rangle$. Moreover, we are interested in the regime where $|\alpha_g| \gtrsim 1$ such that there are two macroscopically distinct ground states. Reactive wave packets that are prepared with

the qubit in $|\pm\rangle$ at any location in phase space should oscillate around the respective ground state [Fig. 2(a)]. We demonstrate this first for an initial vacuum state, which is a displaced state with respect to the minimum of each of the driven potentials. We initialize the driven qubit in $|-\rangle$ and then ramp on two sideband drives quickly with respect to $1/\Omega_R$ with the appropriate phases (see Appendix D). By adjusting the average of the sideband frequencies relative to the Stark-shifted cavity frequency, we tune Δ_a , taking care to satisfy the resonance conditions at each frequency configuration. We observe the resulting dynamics by measuring the projection onto the vacuum state as a function of time using a photon-number-selective π pulse 35]] on a separate transmon ancilla [Fig. 2(b)]. At the same time, we measure $\langle \hat{\sigma}_x \rangle$ of the qubit using our previously described measurement scheme and observe that it largely remains in its initial eigenstate $|-\rangle$ up to decoherence. In the context of the LVC model, we have $\langle \hat{\sigma}_x \rangle = 2 \langle \hat{P}_+ \rangle - 1$ and $\langle \hat{P}_- \rangle = 1 - \langle \hat{P}_+ \rangle$, where $\hat{P}_\pm = |\pm \rangle \langle \pm |$ are projectors onto the diabatic states and $\langle \hat{P}_{\pm} \rangle$ are the corresponding diabatic populations. This demonstrates that we are able

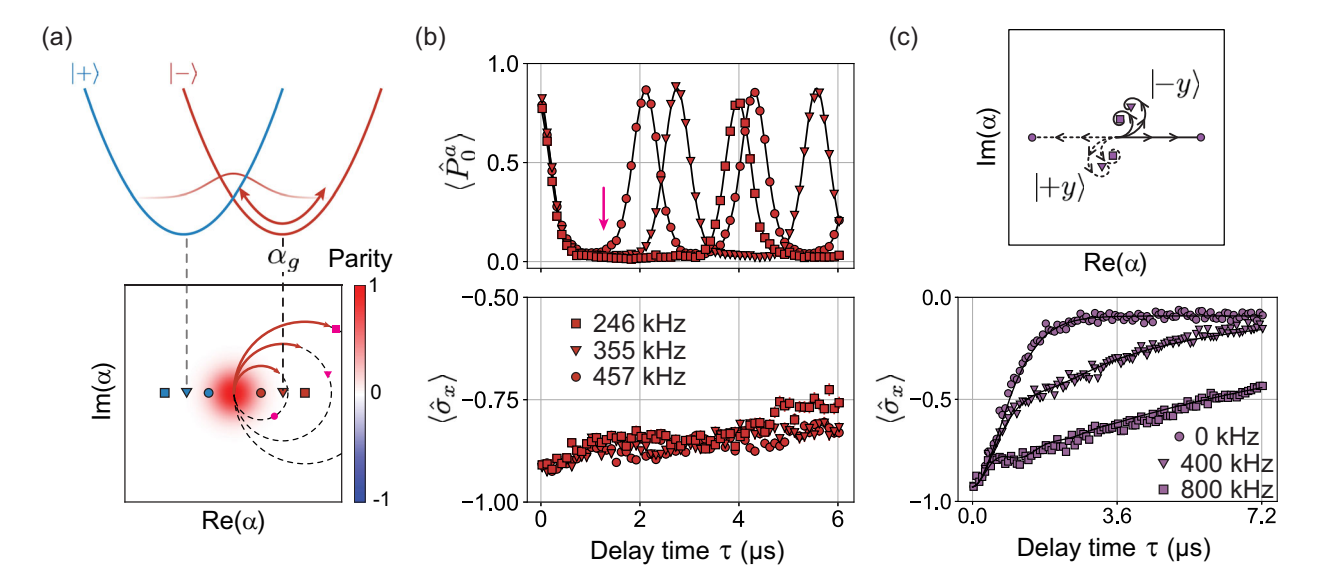


FIG. 2. Calibrating coherent and dissipative conditional displacement interactions on the tuning mode (a),(b) and the coupling mode (c). (a) Depiction of tuning mode dynamics under \hat{H}_a . The oscillator's equilibrium position shifts by $+\alpha_q$ when the qubit is in $|-\rangle$ (red) and $-\alpha_q$ when the qubit is in $|+\rangle$ (blue). Top: an initial wave packet $|-\rangle \otimes |\alpha = 0\rangle_a$ oscillates along the red potential surface associated with $|-\rangle$. Bottom: in phase space, the state performs a circular trajectory around the equilibrium location, indicated by the red triangle for the top schematic. Smaller and larger equilibrium positions are indicated by the circle and square, respectively. (b) Coherent state revivals during evolution under \hat{H}_a . We prepare an initial state $|-\rangle \otimes |\alpha = 0\rangle_a$ and simultaneously measure the vacuum projector of the tuning mode $\hat{P}_0^a = |0\rangle_a \langle 0|_a$ (top) and $\hat{\sigma}_x$ (bottom) for different calibrated values of Δ_a . Solid lines are fits to a simple analytic model, extracting values $g_x/2\pi = 450$ kHz and $\Delta_a/2\pi = 457$ kHz (circles), 355 kHz (triangles), and 246 kHz (squares) which determine the values of α_q . Approximate locations of the coherent state for each calibration at a delay time marked by the magenta arrow are shown in the bottom panel of (a). At the same time, the qubit largely remains in $|-\rangle$ up to intrinsic decoherence. (c) Top: coupling mode state trajectories starting in vacuum $|0\rangle_b$ for various values of Δ_b (rates from the bottom panel) with fixed values of \hat{g}_b and κ_b , splitting in phase space depending on if the qubit is in $|\pm y\rangle$. Full coherent state distributions are not depicted because we are in the weak measurement regime where there is significant overlap between the coherent states. Bottom: measurement-induced dephasing of $|-\rangle$ with $g_y/2\pi \approx 117$ kHz, $\Delta_b/2\pi \approx \{0(\text{circles}), 400(\text{triangles}), 800(\text{squares})\}$ kHz and $\kappa_b/2\pi \approx 320$ kHz obtained from independent calibrations. Solid lines represent equivalent time-domain master equation simulation results (see Appendix F). All error bars indicate standard deviations and may not be visible compared to marker size.

engineer \hat{H}_a with in situ control of the Hamiltonian parameters.

Next, we independently calibrate \hat{H}_b and its dissipative dynamics in the absence of coupling to the tuning mode. From a quantum optics perspective, the combination of a conditional displacement interaction \hat{H}_b and single photon loss with rate $\kappa_b/2\pi \approx 320$ kHz results in measurementinduced dephasing of the qubit along the axes orthogonal to the interaction [36,37]. We verify this behavior by preparing an eigenstate of $\hat{\sigma}_x$, tuning the qubit axis of the interaction to be $\hat{\sigma}_y$ by adjusting the relative phase of the sidebands on the coupling mode (see Appendix B), and measuring $\langle \hat{\sigma}_r \rangle$ as a function of time [Fig. 2(c)]. The measurements reveal dephasing rates that are suppressed when Δ_b increases, as expected. Similar to the interaction on the tuning mode, the conditional displacement strength g_{y} and detuning Δ_{b} can be controlled in situ. Ultimately, this yields a tunable measurement-induced $\hat{\sigma}_{v}$ dephasing with a finite bandwidth, which we will proceed to activate in conjunction with the coherent interaction on the tuning mode. Full experimental calibration details for both interactions $\{\hat{H}_a, \hat{H}_b\}$ are provided in Appendix D.

B. Demonstration of wave-packet branching

Before combining the two conditional displacement interactions to enact $\hat{H}_{\rm LVC}$, we first perform a control experiment to observe branching of a reactive wave packet due to the intrinsic noise of our quantum simulator. Under \hat{H}_a , where the eigenstates of $\hat{\sigma}_x$ determine the two potential surfaces, we define branching of a reactive wave packet to be a process (either coherent or noisy) that flips $|+\rangle \leftrightarrow |-\rangle$, which causes the wave packet to branch to the opposite potential surface [Fig. 3(a)]. Note that this process bears resemblance to trajectory-based surface hopping algorithms [38,39], except that in those algorithms nuclei are treated classically. We can probe this effect, while also simultaneously verifying that we have control over two simultaneous conditional displacement interactions, by enacting the following control Hamiltonian:

$$\hat{H}_x/\hbar = \Delta_a \hat{a}^\dagger \hat{a} + \Delta_b \hat{b}^\dagger \hat{b} + \hat{\sigma}_x [g_x(\hat{a} + \hat{a}^\dagger) + g_y(\hat{b} + \hat{b}^\dagger)]. \tag{4}$$

We engineer \hat{H}_x by adjusting the sideband drive phases to align the interaction of both modes to $\hat{\sigma}_x$ (see Appendix B). In this scenario, the eigenstates of \hat{H}_x are product states in the uncoupled basis $\{|\mp\rangle\otimes\hat{\mathcal{D}}(\pm\alpha_g)|n\rangle_a\otimes\hat{\mathcal{D}}(\pm\beta_g)|n\rangle_b\}$, where dissipation modifies the value of $\beta_g=g_y/\sqrt{\Delta_b^2+\kappa_b^2/4}$ and $\{|n\rangle_{a/b}\}$ are Fock state ladders of each mode. As such, any measurement-induced dephasing from the coupling mode should not perturb the dynamics of a reactive wave packet since they do not cause transitions

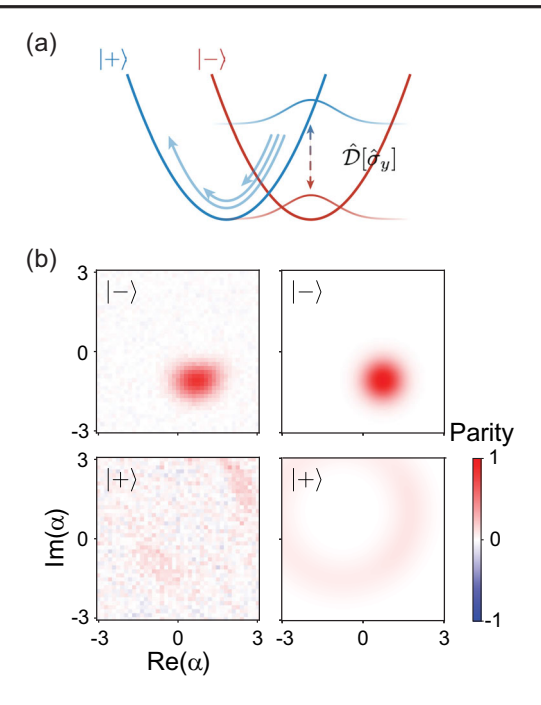


FIG. 3. Wave-packet branching under white noise dephasing. (a) A ground state reactive wave packet $|-\rangle \otimes |\alpha_q\rangle$ branches from the red potential surface to the blue potential surface when a dephasing event flips the electronic qubit from $|-\rangle$ to $|+\rangle$ (and vice versa). When the wave packet branches at random times, it will subsequently evolve along the blue potential surface which diffuses the oscillator state toward a mixed state. (b) Measured (left) and simulated (right) Wigner functions of the tuning mode conditioned on the $\hat{\sigma}_x$ measurement outcome being either $|-\rangle$ (top, $P_{-} = 91\%$) or $|+\rangle$ (bottom, $P_{+} = 9\%$) after evolving $|\psi_0\rangle = |-\rangle \otimes |+\alpha_a\rangle_a \otimes |0\rangle_b$ for 10 µs under \hat{H}_x with the parameters listed in the main text. Experimentally, the overall phase of the measured Wigner functions is determined by the phase acquired by the cavity relative to the initial displacement due to Stark shifts and is free to be adjusted [40]. The phase in the simulation is aligned to that of the coherent projected data $(|-\rangle)$. Additional deviations of the experimental data from the simulation are likely due to higher order Hamiltonian terms, whose precise calibration and control remain an open task left for future experiments.

between $|\pm\rangle$. Thus, our previous description of branching remains valid in the case of white noise and we do not have to consider the dynamics of the coupling mode.

For our control experiment, we enact \hat{H}_x with calibrated parameters $g_x/2\pi=410$ kHz, $\Delta_a/2\pi=324$ kHz, $g_y/2\pi\approx 156$ kHz, and $\Delta_b/2\pi\approx 0$ kHz. We prepare a ground state of the tuning mode $|-\rangle\otimes|+\alpha_g\rangle_a\otimes|0\rangle_b$ (see Appendix D) and let the system evolve under \hat{H}_x for a delay time $\tau=10$ μ s that is short compared to the intrinsic coherence time of the qubit $\tau< T_{2\rho}^x$ (here we label the decoherence with a superscript x to indicate it is measured with \hat{H}_x active). Next, we simultaneously measure the qubit in the $\hat{\sigma}_x$ basis and perform Wigner tomography on the cavity using the ancilla transmon [16]. In the language of

quantum dynamics, the Wigner distribution is function in a phase space that contains full information about the quantum state. The marginal distributions represent wave-packet probability distributions of the tuning mode along position and momentum, which in our case is represented by the real and imaginary components of the electromagnetic field $\{Re(\alpha), Im(\alpha)\}$. Correlating the tomography results with the qubit measurement outcome reveals that the wave packet remains coherent if the qubit did not experience a dephasing event, i.e., stays in $|-\rangle$, or fully dephases otherwise if environmental noise caused a flip from $|-\rangle \rightarrow |+\rangle$ [Fig. 3(b)]. Because the time of each individual dephasing event is unknown to the experimentalist, the oscillator state will be in a uniformly distributed mixed state with constant total energy in the displaced frame (reminiscent of a donut in phase space centered around the opposite ground state). Thus, we have verified that wave-packet branching indeed occurs alongside qubit dephasing in our quantum simulator, and that we are able to faithfully enact two conditional displacement Hamiltonians simultaneously.

C. Dissipative dynamics through a conical intersection

The wave-packet branching observed under \hat{H}_x and a white noise dissipator $(\gamma_{2\rho}^x/2) \times \mathcal{D}[\hat{\sigma}_y]\hat{\rho}$, where $2\pi \times \gamma_{2\rho}^x = 1/T_{2\rho}^x$, largely does not depend on the location of the reactive

wave packet, and thus on the corresponding energy gap $\propto \hat{\sigma}_x$. Under \hat{H}_{LVC} and the conical intersection, this is no longer the case. To demonstrate this, we activate \hat{H}_{LVC} with calibrated parameters $g_x/2\pi = 158.0 \,\text{kHz}$, $\Delta_a/2\pi = 125.8 \,\text{kHz}$, $g_y/2\pi =$ 115 kHz, and $\Delta_b/2\pi \approx 0$ kHz. With our confirmed understanding that qubit dephasing along $\hat{\sigma}_x$ drives wave-packet branching, we prepare the system with reactive wave packets at different locations $|-\rangle \otimes \{|0\rangle_a, |\alpha_q\rangle_a, |2\alpha_q\rangle_a\} \otimes |0\rangle_b$ and directly monitor $\langle \hat{\sigma}_x \rangle$ as a function of time [Fig. 4(a)]. We observe that the qubit dephasing is both highly nonexponential and stronger upon passage of the reactive wave packet through the intersection. Additionally, we further verify that this behavior indeed correlates with dephasing of the cavity state by taking Wigner functions of an initially displaced wave packet before and after passage through the conical intersection. In this instance, we reduce the interaction strengths of the reactive potential surface to get a clear signature of branching over the course of one period of motion, and choose zero detuning on the coupling mode's conditional displacement to achieve the strongest dephasing, representing a very slow intranuclear mode.

In order to qualitatively understand the dissipative dynamics that we observe, we can imagine treating the tuning mode classically. Here, we are left with a simplified Hamiltonian,

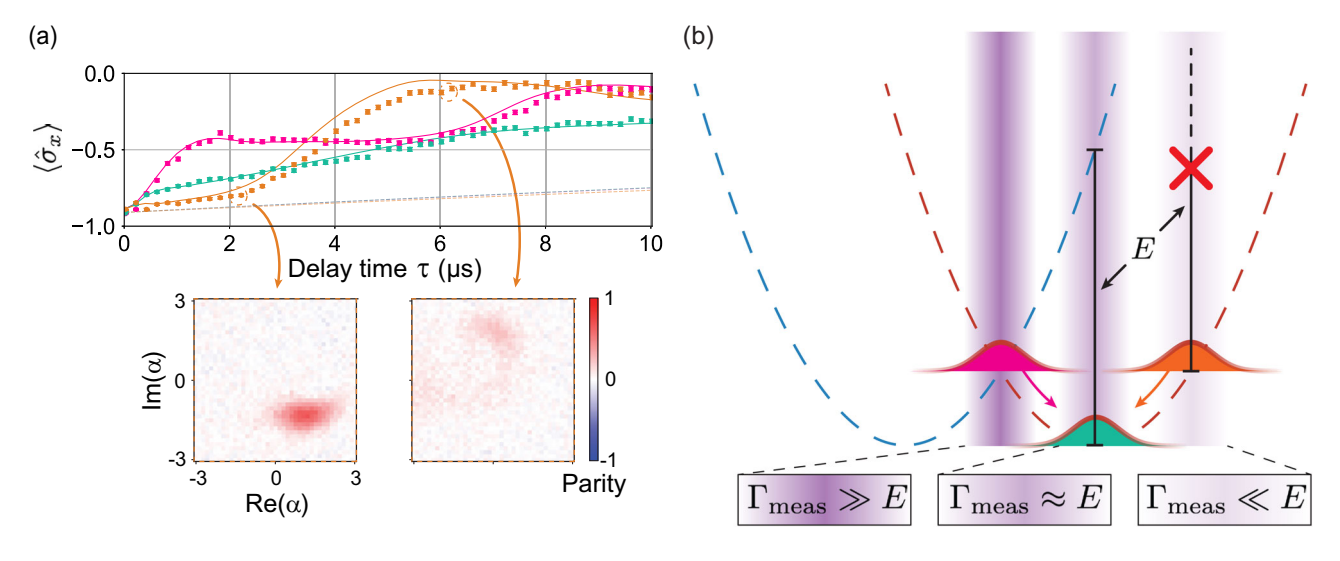


FIG. 4. Branching through a conical intersection. (a) Top: measured expectation value of $\hat{\sigma}_x$ with standard error bars over time for the three different initial states $|-\rangle \otimes |a_0\rangle_a \approx \{|0\rangle_a (\text{magenta}), |\alpha_g\rangle_a (\text{blue green}), |2\alpha_g\rangle_a (\text{orange})\} \otimes |0\rangle_b$, where $\alpha_g = g_x/\Delta_a \approx 1.26$. The magenta wave packet prepared at the CI immediately dephases, whereas the other two dephase more slowly, as they are farther away. After half of an oscillation period $\tau \sim 1/(2\Delta_a)$, the orange wave packet arrives at the CI and dephases. Solid lines are predictions from a master equation simulation using independently fitted parameters. Dashed lines represent the negligible background decoherence due to $T_{2\rho}^x$ on the timescale of the interaction and dissipation. Bottom: unconditional Wigner tomography on the tuning mode at $\tau = 2$ µs (left) and 6 µs (right) for preparing $|\alpha_0\rangle_a \approx |2\alpha_g\rangle_a$, revealing a coherent wave packet before and dephased state after passage through the CI. The distortion of the Wigner function from a Gaussian at $\tau = 2$ µs suggests the presence of a residual self-Kerr nonlinearity in the oscillator. (b) A semiclassical interpretation of the dephasing versus location of the three initial wave packets prepared in (a). The potential surfaces are shown in dashed lines to emphasize that they are no longer exact in the diagonalized basis of \hat{H}_{LVC} . The dissipative dynamics arises from a competition between the $\hat{\sigma}_x$ energy gap E with the finite strength of the dephasing Γ_{meas} .

$$\hat{H}_{\text{Zeno}}/\hbar = E(x)\hat{\sigma}_x + \Delta_b \hat{b}^{\dagger} \hat{b} + g_y \hat{\sigma}_y (\hat{b} + \hat{b}^{\dagger}), \quad (5)$$

subject to single photon loss on mode \hat{b} at a rate κ_h . The function E(x) can be interpreted as the position-dependent energy gap (in frequency units) between qubit states for a conditional displacement interaction. At the CI, i.e., at x = 0, this energy gap vanishes and we are left with the environment measuring $\hat{\sigma}_y$ with a measurement strength $\Gamma_{
m meas}=g_y^2\kappa_b/[(\kappa_b/2)^2+\Delta_b^2]$ in the steady state where $g_v \ll \kappa_b$. Away from the origin, the qubit has a finite energy along an axis orthogonal to that of the measurement and we recover a scenario reminiscent of Zeno dynamics of a driven qubit [41]. This reduces the effective measurement strength, resulting in slower decoherence and thus reduced branching events [Fig. 4(b)]. As such, a semiclassical approximation would correspond to choosing a timedependent trajectory x(t) for an initial Gaussian wave packet. Interestingly enough, this model contains regions in parameter space where the steady-state qubit polarization is not 0.5 as one may naively expect. A full in-depth analysis is provided in Appendix G. In our full model, wave packets in the tuning mode will diffuse in phase space due to the branching, resulting in dynamics that are quantitatively different from the above simplified model.

IV. OUTLOOK

Modifications to our experimental setup can be made to expand the scope of dynamics in our LVC model. For instance, by overcoupling the tuning mode to a transmission line, the reactive coordinate will experience dissipation which would eventually localize an initially excited wave packet into the two ground states and define a branching ratio. The addition of κ_a as a tuning knob, particularly in the regime $\kappa_a \sim \kappa_b$, expands the landscape of competing forces in our model and represents a more realistic description of a reaction. We note the possibility of tuning the decay rate of each oscillator *in situ* via mechanical means in our 3D architecture, which would enable a flexible way to explore the wider range of parameter space.

On a broader scale, it will be necessary to both scale up our simulator and add complexity to our model in order to simulate larger molecules and challenge classical methods. As described in Appendix B, our method of enacting $\hat{H}_{\rm LVC}$ can easily be extended to existing multimode systems where a large number of cavity modes (~10) are dispersively coupled to a single transmon, such as in Refs. [14,15].

Expanding from the LVC model to include higher order couplings, however, will require the development of new control techniques that have yet to be proposed for any system. This would allow for a more accurate modeling of realistic systems, whose dynamics are heavily influenced by nuclear topography. The flexibility of engineering the Josephson potential to enact mixing processes of various

orders poses promise for this task [42,43]. Furthermore, systems that have Franck-Condon regions far from the CI will translate to larger photon numbers in our simulator. As such, precisely controlling the desired nonlinear reaction Hamiltonian over the domain of larger photon numbers will be a central challenge to address in future experiments.

Beyond quantum chemistry, the successful implementation of our quantum simulator motivates the investigation of novel cavity QED physics [44,45]. The primary advantage of our approach is the *in situ* tunability of the constituent interactions in a quantum simulator to explore system dynamics in various parameter regimes.

V. CONCLUSION

In summary, our results highlight the interplay between coherent evolution and engineered dissipation in a system whose energy landscape contains a CI. We achieve this via careful Hamiltonian engineering of a circuit QED processor involving five simultaneous microwave drives and engineered dissipation, along with the appropriate state preparation and measurement protocols to observe branching dynamics. In particular, branching events arise when dissipation in the coupling mode induces flips on the electronic state and correspondingly causes the reactive wave packet to jump onto the opposite potential surface. These branching events are at the heart of chemical reaction dynamics, such as the cis-trans isomerization reaction of rhodopsin [46], a central process in human vision, and occur more frequently upon passage through the CI. Our experiment demonstrates and further confirms the immense flexibility of this platform to perform quantum information processing tasks by dressing microwave modes with continuous drives [33,47,48], and constitutes an important step toward investigating more complex chemical phenomena with higher degrees of accuracy. It is worth noting that the techniques developed in our work may readily be applicable to control multimode bosonic systems coupled to one or a few qubits [15,49]. Looking ahead, incorporating additional features into our simulator such as additional controlled nonlinearities and structured dissipators, while scaling up the number of electronic states and rovibrational modes, will enable more accurate simulation of larger molecules. More broadly, this expands the landscape of controllable qubit-oscillator interactions in a circuit OED platform, which may be useful for bosonic quantum computation, error correction, and simulation.

ACKNOWLEDGMENTS

We acknowledge the early insight of V. Batista for simulating conical intersections. We thank A. Eickbusch, R. G. Cortiñas, A. Koottandavida, and L. Frunzio for helpful experimental discussions. We acknowledge Y. Gao and B. Lester for initial package design. Facilities use was supported by YINQE and the Yale SEAS

cleanroom. This research is supported by the U.S. Army Research Office (ARO) under Grant No. W911NF-18-1-0212. The views and conclusions contained in this document are those of the authors and should not be interpreted as representing the official policies, either expressed or implied, of the ARO, or the U.S. Government. The U.S. Government is authorized to reproduce and distribute reprints for Government purposes notwithstanding any copyright notation thereon. S. P. acknowledges support from the National Science Foundation (QLCI Grant No. OMA-2120757). We also acknowledge support of the Yale Quantum Institute.

C. S. W., M. H. D., and R. J. S. conceived the experiment. C. S. W. and N. E. F. performed early stage experimental design. C. S. W. and B. J. C. fabricated the qubits and assembled the device. C. S. W. developed the experimental protocol, performed measurements, and carried out numerical simulations with N. E. F., B. J. C., and R. J. S providing input. S. P. and S. M. G. provided theoretical support. C. S. W. and R. J. S. wrote the paper with feedback from all authors.

APPENDIX A: CONSTRUCTING A DIABATIC HAMILTONIAN CONTAINING A CONICAL INTERSECTION

In this appendix, we describe the general formalisms behind obtaining various model and/or *ab initio* molecular Hamiltonians that involve strong vibronic coupling. We begin with a brief review of adiabatic potential energy surfaces and highlight the difficulties that arise in the vicinity of conical intersections. This motivates the use of diabatic electronic states, which form the basis of the Hamiltonians that we consider [50].

The standard molecular Hamiltonian is

$$\hat{H}_{\text{mol}} = \hat{T}_n(\partial_{\vec{R}}) + \underbrace{\hat{T}_e(\partial_{\vec{r}}) + \hat{V}(\vec{r}, \vec{R})}_{\hat{H}_e}, \tag{A1}$$

where \hat{T} and \hat{V} correspond to kinetic and Coulomb potential energies, respectively, and the subscripts n and e denote nuclei and electrons. \vec{r} and \vec{R} represent the positions of the electrons and nuclei, respectively.

The conventional approach based on the Born-Oppenheimer approximation begins with noting that the electron masses m_e are much smaller than the nuclear masses m_N . This motivates momentarily dropping $\hat{T}_n(\partial_{\vec{R}}) \propto 1/m_N$ altogether, leaving behind a reduced Hamiltonian of the electrons only with parametric dependence on the nuclear coordinates \vec{R} . By choosing an ansatz for the total molecular wave function $\Psi(\vec{r}, \vec{R}) = \Sigma_i \varphi_i(\vec{r}, \vec{R}) \chi_i(\vec{R})$, we get a reduced electronic Schrodinger equation:

$$\hat{H}_e \varphi_i(\vec{r}, \vec{R}) = E_i(\vec{R}) \varphi_i(\vec{r}, \vec{R}), \tag{A2}$$

where $E_i(\vec{R})$ is the potential energy surface for the *i*th electronic eigenstate. Here, we have identified a complete set of adiabatic electronic eigenfunctions $\varphi_i(\vec{r}, \vec{R})$. Returning to the full Schrodinger equation,

$$\hat{H}_{\text{mol}}\Psi(\vec{r},\vec{R}) = [\hat{T}_n(\partial_{\vec{R}}) + \hat{H}_e] \sum_i \varphi_i(\vec{r},\vec{R}) \chi_i(\vec{R}), \quad (A3)$$

we can obtain a reduced equation for the nuclear motion by integrating over a complete set of adiabatic electronic eigenfunctions $\varphi_i^*(\vec{r}, \vec{R})$. This brings out terms such as

$$\frac{\langle \varphi_j(\vec{r}, \vec{R}) | \hat{\nabla}_R \hat{H}_e | \varphi_i(\vec{r}, \vec{R}) \rangle}{E_j(\vec{R}) - E_i(\vec{R})},\tag{A4}$$

which arise from the application of $\hat{T}_n(\partial_{\vec{R}}) \propto -(1/2m_N)\hat{\nabla}_R^2$ on $\varphi_i(\vec{r},\vec{R})$. These are commonly referred to as nonadiabatic coupling terms in the literature. It is clear that in the vicinity of a conical intersection, these terms diverge as the denominator becomes very small and the adiabatic electronic basis fails to be an appropriate basis for calculations and analyses.

Given the aforementioned issue, one can consider instead a diabatic electronic basis $\phi_k(\vec{r})$ such that the molecular wave function can be expressed as

$$\Psi(\vec{r}, \vec{R}) = \sum_{k} \phi_{k}(\vec{r}) \chi_{k}'(\vec{R}), \tag{A5}$$

where the diabatic states are, by definition, diagonal in the nuclear kinetic energy operator. Off-diagonal couplings between electronic states must of course exist, but now they arise via the potential $\langle \phi_j | \hat{V}(\vec{r}, \vec{R}) | \phi_i \rangle$ and do not involve wave-function derivatives.

This forms the basis for a general vibronic coupling Hamiltonian:

$$\hat{H}_{\rm VC} = \sum_{n} |\phi_n\rangle [\hat{T}_n + W_{nn}(\vec{R})] \langle \phi_n| + \sum_{n\neq m} |\phi_n\rangle W_{nm}(\vec{R}) \langle \phi_m|. \eqno({\rm A6})$$

In our experiment, we consider a minimal model for a twodimensional linear vibronic coupling Hamiltonian, where we have for two normal modes:

$$\hat{T}_n = \frac{\hat{P}_t^2}{2m_t} + \frac{\hat{P}_c^2}{2m_c},\tag{A7}$$

$$\hat{W} = \begin{pmatrix} \sum_{i=t,c} \frac{1}{2} m_i \Delta_i^2 \hat{Q}_i^2 + g_x \hat{q}_t & g_y \hat{q}_c \\ g_y \hat{q}_c & \sum_{i=t,c} \frac{1}{2} m_i \Delta_i^2 \hat{Q}_i^2 - g_x \hat{q}_t \end{pmatrix},$$
(A8)

with momentum $\hat{P}_{t/c}$ and position $\hat{Q}_{t/c}$ with effective masses $m_{t/c}$ and frequencies $\Delta_{t/c}$, respectively. By recasting these coordinates into dimensionless creation and annihilation operators,

$$\hat{P}_{t/c} = p_{\text{ZPF}}^{t/c} \hat{p}_{t/c}, \tag{A9}$$

$$\hat{Q}_{t/c} = q_{\mathsf{ZPF}}^{t/c} \hat{q}_{t/c},\tag{A10}$$

where $\hat{p}_t = i(\hat{a}^\dagger - \hat{a})$, $\hat{p}_c = i(\hat{b}^\dagger - \hat{b})$, $\hat{q}_t = \hat{a} + \hat{a}^\dagger$, $\hat{q}_c = \hat{b} + \hat{b}^\dagger$, and $q_{\text{ZPF}}^i = \sqrt{\hbar/2m_i\Delta_i}$, $p_{\text{ZPF}}^i = \sqrt{\hbar m_i\Delta_i/2}$ for $i \in \{t,c\}$, we arrive at \hat{H}_{LVC} [Eq. (3) of the main text].

APPENDIX B: ENGINEERING CONDITIONAL DISPLACEMENTS

Here, we describe how we engineer the conditional displacement interactions that make up \hat{H}_{LVC} . As discussed in the main text, this Hamiltonian consists of two simultaneous conditional displacement interactions $\{\hat{H}_a, \hat{H}_b\}$ of a single qubit to two different cavity modes, where the qubit coupling axes are orthogonal. To simplify the derivation, we will begin by focusing on how we enact just one of these interactions. As we will see, adding additional interactions to other cavity modes is relatively straightforward, and the qubit coupling axis is freely adjustable in the effective x-y plane.

We expand upon the derivation provided by Ref. [33] by incorporating the finite anharmonicity of the transmon mode. We begin with the static Hamiltonian of a transmon mode \hat{q} dispersively coupled to a cavity mode \hat{c} :

$$\hat{H}_{\rm static}/\hbar = \omega_c \hat{c}^\dagger \hat{c} + \omega_q \hat{q}^\dagger \hat{q} - \frac{\alpha_q}{2} \hat{q}^\dagger \hat{q}^\dagger \hat{q} \, \hat{q} - \chi \hat{c}^\dagger \hat{c} \hat{q}^\dagger \hat{q}, \quad (\text{B1})$$

where α_q is the transmon anharmonicity and χ is the dispersive shift. At a high level, we will see that the conditional displacement interaction arises by transforming the cross-Kerr interaction between the transmon and the cavity. Thus, our approach will be to consider how driving each mode transforms the static interaction. Specifically, we drive the system with one tone coupled to the transmon and two coupled to the cavity:

$$\begin{split} \hat{H}_d/\hbar &= 2\varepsilon_R \cos[(\omega_q + \Delta_R)t](\hat{q} + \hat{q}^\dagger) \\ &- 2i\varepsilon_1 \sin(\omega_1 t + \varphi_1)(\hat{c} - \hat{c}^\dagger) \\ &- 2i\varepsilon_2 \sin(\omega_2 t + \varphi_2)(\hat{c} - \hat{c}^\dagger), \end{split} \tag{B2}$$

such that the full system Hamiltonian is described by $\hat{H}=\hat{H}_{\rm static}+\hat{H}_d$. For convenience, we regroup the terms such that we can write $\hat{H}=\hat{H}_q(\hat{q},\hat{q}^\dagger)+\hat{H}_c(\hat{c},\hat{c}^\dagger)+\hat{H}_{\rm int}$, where $\hat{H}_{\rm int}/\hbar=-\chi\hat{c}^\dagger\hat{c}\hat{q}^\dagger\hat{q}$. We first go into the rotating

frame of the transmon drive via $\hat{H} \rightarrow \hat{U} \hat{H} \hat{U}^{\dagger} + i \hat{U} \hat{U}^{\dagger}$, where $\hat{U} = e^{i(\omega_q + \Delta_R)t\hat{q}^{\dagger}\hat{q}}$:

$$\hat{H}/\hbar = \underbrace{-\Delta_R \hat{q}^{\dagger} \hat{q} - \frac{\alpha_q}{2} \hat{q}^{\dagger} \hat{q}^{\dagger} \hat{q} \hat{q} + \varepsilon_R (\hat{q} + \hat{q}^{\dagger})}_{\hat{H}_q/\hbar} + \hat{H}_c/\hbar - \chi \hat{c}^{\dagger} \hat{c} \hat{q}^{\dagger} \hat{q}, \tag{B3}$$

noting that we have performed the rotating wave approximation and discarded terms rotating at $\mathcal{O}(\omega_q)$. Furthermore, the cross-Kerr term remains unaffected since it is proportional to $\hat{q}^{\dagger}\hat{q}$. Now, we diagonalize \hat{H}_q and reexpress it in the resulting eigenbasis:

$$\hat{H}_q/\hbar = \sum_i \epsilon_i |i\rangle\langle i|, \tag{B4}$$

where we label $i \in \{+, -, \tilde{f}, \ldots\}$ in correspondence with the fact that we will be working in a regime where the two lowest driven eigenstates strongly resemble those of a standard qubit that is driven on resonance, but now incorporate a weak dressing with higher levels of the transmon. We identify the Rabi frequency to be the energy difference between the lowest two eigenstates $e_+ - e_- = \Omega_R$ and define an effective anharmonicity as $e_- - e_{\tilde{f}} = \Omega_R + \tilde{\alpha}$. At this stage, we turn to numerics and construct a unitary basis transformation between the undriven and driven transmon eigenstates for a finite truncation of the transmon Hilbert space. We then reexpress the cross-Kerr interaction in the driven basis, giving us

$$\hat{H}/\hbar = \sum_{i} \epsilon_{i} |i\rangle\langle i| + \hat{H}_{c}/\hbar - \chi \hat{c}^{\dagger} \hat{c} \sum_{ik} u_{jk} |j\rangle\langle k|. \quad (B5)$$

We can further simplify this by going into the frame of the driven transmon $\hat{U}=e^{i\hat{H}_qt/\hbar}$, which performs the transformations $|j\rangle \to e^{i\epsilon_jt/\hbar}|j\rangle$, resulting in

$$\hat{H}/\hbar = \hat{H}_c/\hbar - \chi \hat{c}^{\dagger} \hat{c} \underbrace{\sum_{jk} u_{jk} e^{i(\epsilon_j - \epsilon_k)t/\hbar} |j\rangle\langle k|}_{\hat{a}\hat{t}\hat{a}}, \qquad (B6)$$

where $u_{jk} = u_{kj}^*$. We consider the terms associated with the lowest three levels explicitly:

$$\begin{split} \hat{q}^{\dagger}\hat{q} &= u_{++}|+\rangle\langle+|+u_{--}|-\rangle\langle-|+u_{\tilde{f}\tilde{f}}|\tilde{f}\rangle\langle\tilde{f}| \\ &+ u_{+-}e^{i\Omega_{R}t}|+\rangle\langle-|+u_{-+}e^{-i\Omega_{R}t}|-\rangle\langle+| \\ &+ u_{-\tilde{f}}e^{i(\Omega_{R}+\tilde{\alpha})t}|-\rangle\langle\tilde{f}|+u_{\tilde{f}-}e^{-i(\Omega_{R}+\tilde{\alpha})t}|\tilde{f}\rangle\langle-| \\ &+ u_{+\tilde{f}}e^{i(2\Omega_{R}+\tilde{\alpha})t}|+\rangle\langle\tilde{f}|+u_{\tilde{f}+}e^{-i(2\Omega_{R}+\tilde{\alpha})t}|\tilde{f}\rangle\langle+|. \end{split} \tag{B7}$$

At this stage, we pause and turn to simplify \hat{H}_c . First, we choose to parametrize the two drive frequencies $\omega_{1/2} = \omega_c - \Delta_c \mp \Omega_R$. By going into the rotating frame

at the average of the drive frequencies $\hat{U}=e^{i(\omega_c-\Delta_c)t\hat{c}^{\dagger}\hat{c}}$, we arrive at

$$\begin{split} \hat{H}/\hbar &= \hat{H}_{\rm int}/\hbar + \Delta_c \hat{c}^{\dagger} \hat{c} - \varepsilon_1 (\hat{c} e^{-i\Omega_R t + i\varphi_1} + \hat{c}^{\dagger} e^{i\Omega_R t - i\varphi_1}) \\ &- \varepsilon_2 (\hat{c} e^{i\Omega_R t + i\varphi_2} + \hat{c}^{\dagger} e^{-i\Omega_R t - i\varphi_2}). \end{split} \tag{B8}$$

Finally, we assume that the drive strengths are equal $\varepsilon_2 = -\varepsilon_1 = \varepsilon$ and parametrize the drive phases as their sum and differential components $\varphi_{\Sigma} = (\varphi_1 + \varphi_2)/2$ and $\varphi_{\delta} = (\varphi_1 - \varphi_2)/2$. This allows us to further simplify our Hamiltonian to

$$\hat{H}/\hbar = \hat{H}_{\text{int}}/\hbar + \Delta_c \hat{c}^{\dagger} \hat{c} - 2i\varepsilon \sin(\Omega_R t - \varphi_{\delta})$$

$$\times (\hat{c}e^{i\varphi_{\Sigma}} - \hat{c}^{\dagger}e^{-i\varphi_{\Sigma}}).$$
(B9)

We can observe here that the sum phase of the two sidebands contributes simply as a static rotation of \hat{c} ; therefore we can always align to this frame by experimentally adjusting this phase. Hence, we will set $\varphi_{\Sigma}=0$ here on out to simplify our expressions. At this stage, we aim to eliminate this time-dependent drive term by performing a displacement transformation $\hat{U}=e^{\xi(t)\hat{c}^{\dagger}-\xi^{*}(t)\hat{c}}$. This is achieved by choosing $\xi(t)=(2\varepsilon/\Omega_{R})\cos(\Omega_{R}t+\varphi_{\delta})=\xi_{0}(e^{i(\Omega_{R}t+\varphi_{\delta})}+e^{-i(\Omega_{R}t+\varphi_{\delta})}),$ where $\xi_{0}=(\varepsilon/\Omega_{R}),$ which also transforms $\hat{c}\to\hat{c}+\xi(t).$ This gives

$$\begin{split} \hat{H}/\hbar &= \Delta_{c} [\hat{c}^{\dagger} + \xi^{*}(t)] [\hat{c} + \xi(t)] \\ &- \chi [\hat{c}^{\dagger} + \xi^{*}(t)] [\hat{c} + \xi(t)] \sum_{jk} u_{jk} e^{i(\epsilon_{j} - \epsilon_{k})t/\hbar} |j\rangle\langle k| \\ &= \Delta_{c} [\hat{c}^{\dagger} \hat{c} + \xi(t)(\hat{c} + \hat{c}^{\dagger}) + \xi_{0}^{2}] \\ &- \chi [\hat{c}^{\dagger} \hat{c} + \xi_{0}(e^{i(\Omega_{R}t + \varphi_{\delta})} + e^{-i(\Omega_{R}t + \varphi_{\delta})})(\hat{c} + \hat{c}^{\dagger}) + \xi_{0}^{2}] \\ &\times \sum_{jk} u_{jk} e^{i(\epsilon_{j} - \epsilon_{k})t/\hbar} |j\rangle\langle k|. \end{split} \tag{B10}$$

By substituting the expansion for $\hat{q}^{\dagger}\hat{q}$, discarding terms that rotate at Ω_R and higher, and neglecting constant offsets, we are left with an effective static interaction Hamiltonian:

$$\begin{split} \hat{H}/\hbar &= \Delta_c \hat{c}^\dagger \hat{c} \\ &- \chi \xi_0 u_{+-} (e^{-i\varphi_\delta}|+\rangle \langle -|+e^{i\varphi_\delta}|-\rangle \langle +|) (\hat{c}+\hat{c}^\dagger) \\ &- \chi \hat{c}^\dagger \hat{c} (u_{++}|+\rangle \langle +|+u_{--}|-\rangle \langle -|+u_{\tilde{f}\,\tilde{f}}|\tilde{f}\rangle \langle \tilde{f}|). \end{split} \tag{B11}$$

Importantly, this approximation requires larger Rabi frequencies as we drive harder to induce larger desired interaction strengths (see Appendix B 1). Finally, by neglecting the final term (see Appendix B 2), we arrive at the conditional displacement Hamiltonian between the transmon and one cavity mode:

$$\hat{H}/\hbar = \Delta_c \hat{c}^{\dagger} \hat{c} - g[\cos(\varphi_{\delta})\hat{\sigma}_x + \sin(\varphi_{\delta})\hat{\sigma}_y](\hat{c} + \hat{c}^{\dagger}), \quad (B12)$$

where $g = \chi \xi_0 u_{+-} \approx (\chi \xi_0/2)$ and we have defined our Pauli operators such that $\hat{\sigma}_z = |+\rangle \langle +|-|-\rangle \langle -|$. Here, we have formally identified the qubit that we will use within the larger driven transmon Hilbert space. As we can see, the coupling axis of the qubit fully depends on the differential phase φ_δ of the cavity sidebands relative to the qubit phase (which we have defined as zero here), which can be easily adjusted experimentally without invoking additional Hamiltonian terms. Note that throughout our derivations, we have assumed no accidental frequency collisions that bring unintended Hamiltonian terms into resonance, as would for instance occur if the magnitude of the Rabi frequency Ω_R approaches the magnitude of the transmon anharmonicity α_g .

This scheme extends relatively straightforwardly to multiple cavity modes dispersively coupled to the same transmon. Incorporating a pair of sidebands on each additional cavity is sufficient to activate a conditional displacement involving the driven transmon, as long as the resonance condition is satisfied. It is also worth noting that we have assumed that each sideband couples only to a single cavity mode—in practice, finite crosstalk complicates the calibration procedure of activating all sidebands together. In our experiment, we enact the aforementioned Hamiltonian Eq. (B12) for two cavity modes $\hat{c} \in \{\hat{a}, \hat{b}\}$ coupled to orthogonal axes of the qubit.

1. Optimizing the static cross-Kerr

Here, we consider Eq. (B10) and ask the following questions. How large do we need the Rabi frequency to be in order to safely discard all the rotating terms? Does the answer to this question inform any design choices with regard to our static Hamiltonian? To answer these questions, we first consider all of the different terms that rotate at Ω_R , neglecting any phases:

$$[\Delta_c \xi_0(\hat{c}+\hat{c}^\dagger) - \chi u_{+-} \hat{c}^\dagger \hat{c} \hat{\sigma}_\mp - \chi \xi_0^2 u_{+-} \hat{\sigma}_\mp] e^{\pm i\Omega_R t}.$$

Note that there are also terms that rotate at $\tilde{\alpha}$, $2\Omega_R$, $\Omega_R + \tilde{\alpha}$, $2\Omega_R + \tilde{\alpha}$, and $3\Omega_R + \tilde{\alpha}$, but since the prefactors will all be of the same order, we consider the smallest rotating frequency for the most stringent condition. Importantly, we also require that $\tilde{\alpha} > \Omega_R$, otherwise other terms involving $|\tilde{f}\rangle$ will be activated and we can no longer restrict ourselves to a qubit subspace. This sets a limit on how large of a Rabi frequency can be used for a fixed anharmonicity α_q . The above terms reveal that our conditions for the RWA are

$$\Omega_R \gg \left\{ \Delta_a |\xi_0 \langle (\hat{c} + \hat{c}^\dagger) \rangle |, \frac{\chi}{2} \langle \hat{c}^\dagger \hat{c} \rangle, \frac{\chi}{2} \xi_0^2 \right\},$$
 (B13)

which notably depends on the state of the cavity. It is clear from this that as the conditional displacement interaction strength $g \approx (\chi \xi_0/2)$ increases, the approximation becomes less valid. However, we can instead rewrite the condition for a fixed g:

$$\Omega_R \gg \left\{ \Delta_a |\xi_0 \langle (\hat{c} + \hat{c}^\dagger) \rangle|, \frac{g}{\xi_0} \langle \hat{c}^\dagger \hat{c} \rangle, g\xi_0 \right\},$$
(B14)

which reveals that there is indeed an optimal value for ξ_0 given a fixed g. For considering photon numbers $\langle \hat{c}^{\dagger} \hat{c} \rangle \sim \mathcal{O}(1)$ and $g \approx \Delta_c$, we best satisfy all these conditions by choosing $\xi_0 \approx 1$. This, in turn for a fixed g, suggests that we should roughly target a static cross-Kerr strength of $\chi \approx 2g$.

2. Choice of static detuning of the Rabi drive

The final term in Eq. (B11) represents an effective cross-Kerr interaction between cavity photons and the driven transmon eigenstates. For a true two-level system driven on resonance, which is a good approximation for transmons in the regime that the Rabi frequency is much weaker than the anharmonicity $\Omega_R \ll \alpha_q$, one finds that $u_{++} = u_{--} = 1/2$, which results in a static frequency shift of the cavity and hence a nulled cross-Kerr. As the Rabi frequency Ω_R approaches the anharmonicity α_q , however, $u_{++} \neq u_{--}$ for a drive that is on resonance owing to the hybridization of the driven eigenstates with higher energy levels of the transmon. This results in a residual cross-Kerr which can be interpreted as a slight shift in the Rabi frequency due to the presence of photons in the cavity. This is problematic as it both changes the resonance condition of the interaction and biases our measurement scheme as a function of the cavity photon distribution.

By adding an additional static detuning knob Δ_R on the Rabi drive, we can determine an optimal working configuration that nulls this effective cross-Kerr. We show this optimization in Fig. 5. The presence of this static detuning thus dictates that we perform an adiabatic preparation of our driven qubit eigenstates. This has the further benefit of eliminating leakage events associated with large Rabi

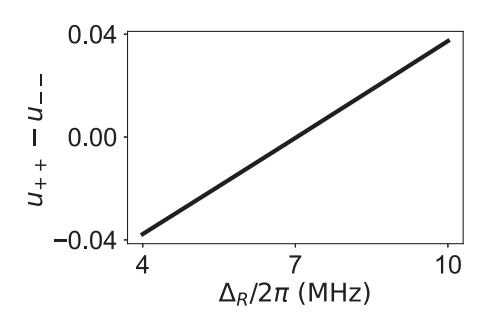


FIG. 5. Optimizing the static detuning. By numerically diagonalizing \hat{H}_q/\hbar for various values of Δ_R , we can plot the dimensionless factor that contributes to the residual cross-Kerr for $\Omega_R/2\pi=80$ MHz and $\alpha_q/2\pi=244$ MHz. We find an optimal value of $\Delta_R/2\pi\approx7$ MHz.

frequencies and finite transmon anharmonicity, but has an additional challenge which we address in Appendix D 5.

APPENDIX C: EXPERIMENTAL DETAILS

A list of the static system parameters is given in Table I. A schematic of the wiring diagram for this experiment is depicted in Fig. 6. We comment below on notable features not explicitly shown in the wiring diagram.

1. Wiring diagram

A field-programmable gate array-based quantum controller synchronizes multiple modules that contain DACs and ADCs for generating the pulses (I and Q control) and digitizing the readout signals, respectively. rf switches are only open while pulses are played on a corresponding mode. The control line for the tuning mode is split between the resonant drive (left) and sideband pumps (right), which are never played simultaneously; thus a closed loop where both rf switches are open together is never formed. The band-stop filter on the pump line is centered on the tuning mode's resonance frequency, suppressing pump-induced noise that may lead to heating of the cavity mode. dc blocks are placed around each active component, as well as on each line at the boundary of the cryostat (i.e., the line separating 300 and 4 K in the schematic). All components in the 20 mK region are thermally anchored to the mixing chamber plate via OFHC copper braids. We use Josephson Parametric Converters (JPCs) as quantum limited amplifiers—only coupling to the signal port is shown.

2. Temperature stabilization

As the derivations of Appendix B suggest, the resonance condition for enacting our reaction Hamiltonian [Eq. (3) of the main text] relies on matching the sideband detunings to the Rabi frequency. The Rabi frequency depends linearly

TABLE I. List of static system parameters.

System quantity	Parameter	Value	
Transmon frequency	$\omega_q/2\pi$	4850 MHz	
Transmon anharmonicity	$\alpha_q/2\pi$	244 MHz	
Transmon relaxation	T_1^q	80 μs	
Transmon decoherence	$T_2^{\dot{q}}$	7 μs	
Tuning mode frequency	$\omega_a/2\pi$	5436 MHz	
Tuning mode linewidth	$\kappa_a/2\pi$	0.23 kHz	
Coupling mode frequency	$\omega_b/2\pi$	6506 MHz	
Coupling mode linewidth	$\kappa_b/2\pi$	320 kHz	
Tuning mode-Transmon coupling	$\chi_{aq}/2\pi$	295 kHz	
Coupling mode–Transmon coupling	$\chi_{bq}/2\pi$	210 kHz	
Ancilla frequency	$\omega_{qa}/2\pi$	4509 MHz	
Ancilla relaxation	T_1^{qa}	60 μs	
Ancilla decoherence	T_2^{qa}	10 μs	
Tuning mode-Ancilla coupling	$\chi_{a,qa}/2\pi$	845 kHz	

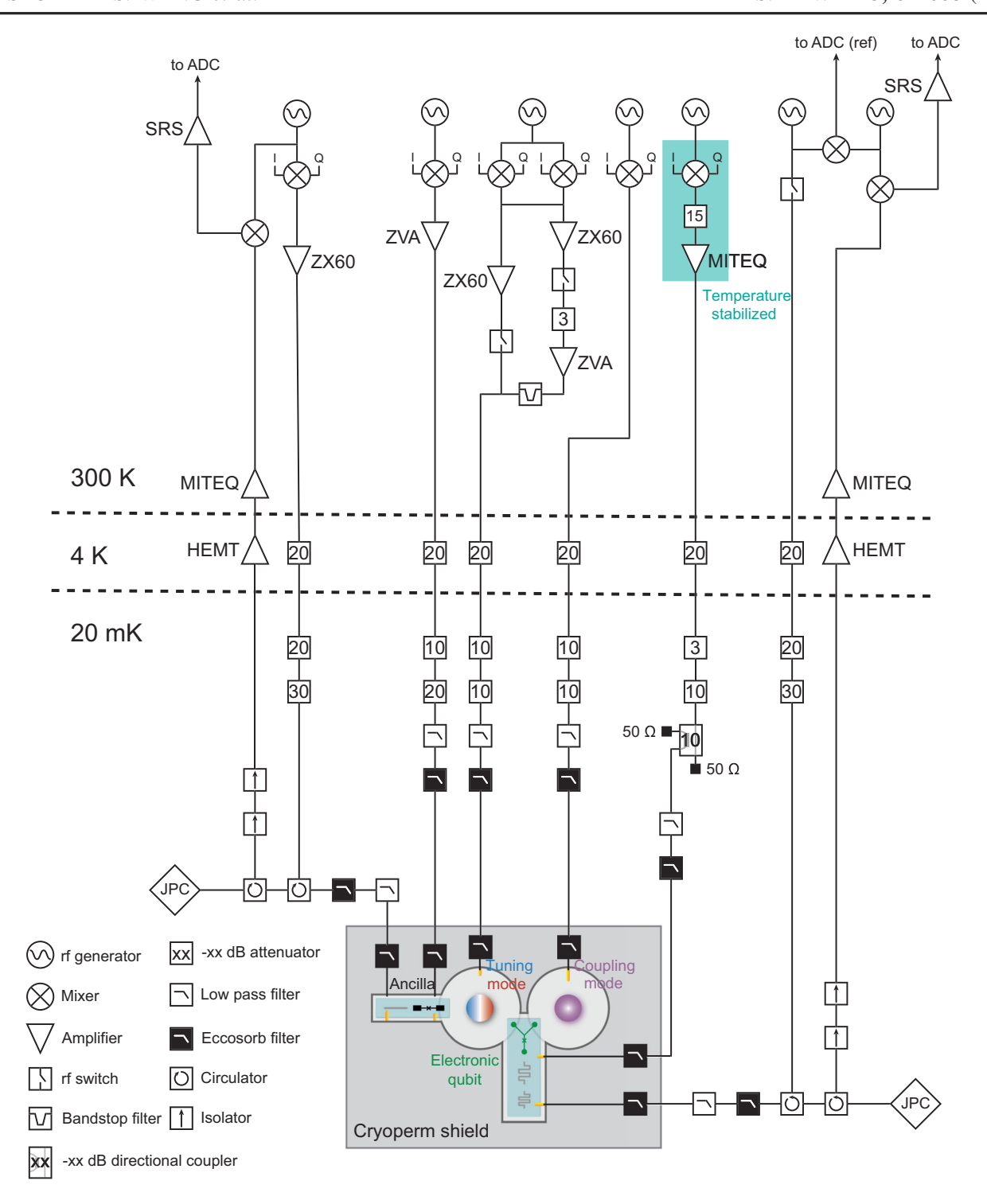


FIG. 6. Experimental wiring diagram.

on the amplitude of the Rabi drive [roughly speaking, using the two-level approximation that $\Omega_R = \sqrt{\epsilon_R^2 + \Delta_R^2}$ and we operate in a regime where $\epsilon_R \gg \Delta_R$, resulting in $\Omega_R \approx \epsilon_R [1 + (\Delta_R^2/2\epsilon_R^2)]]$, and thus is susceptible to amplitude fluctuations such as those caused by variations in the gain at any stage of our microwave control chain. A dominant source of these variations is due to ambient

temperature fluctuations in the lab. To this end, we suppress these fluctuations by anchoring the components (particularly a Marki LXP IQ mixer and MITEQ low noise amplifier; see turquoise box in Fig. 6) to a Thorlabs optical breadboard and placing the breadboard in a cardboard box. We then actively stabilize the temperature of the air in the box via an op-amp-based proportional-integral-derivative

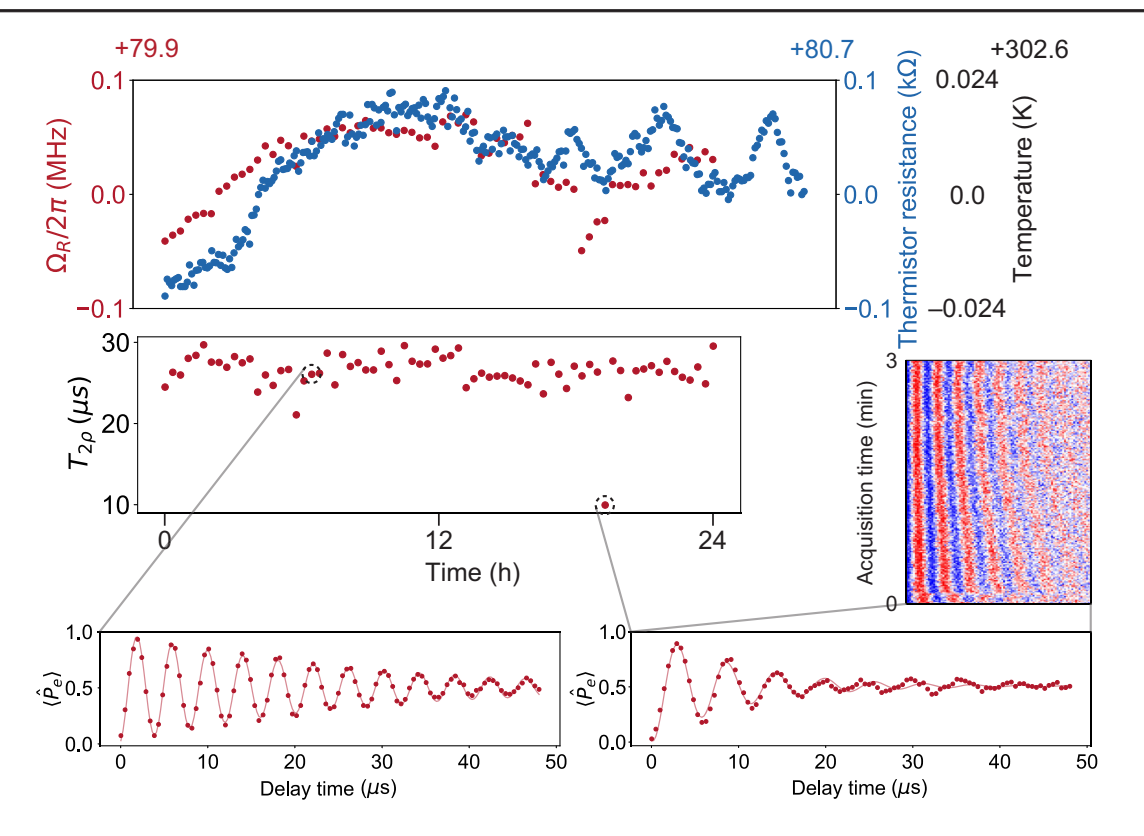


FIG. 7. Tracking system stability over time. Top panel: simultaneous measurements of the Rabi frequency and the ambient temperature (inferred from the measured thermistor resistance) where the active microwave components are held. The data shows that the two are correlated. Middle panel: extracting driven coherences $T_{2\rho}$ suggests a stable amplitude noise spectrum within an acquisition time $\tau_{\rm acq}=3\,$ min (bottom left-hand panel: a typical time-domain Ramsey trace), with a single instance where the amplitude drift was large (bottom right-hand panel), as confirmed via looking at the raw data binned 10 shots at a time over $\tau_{\rm acq}$.

feedback controller that heats an Ohmite ceramic resistor $(R=2.5~\Omega)$ based on a differential measurement of the temperature using a 100 kΩ thermistor referenced to a set point. Figure 7 shows the typical performance of our stabilization and correlates the temperature variations with the amplitude variations as measured via the Rabi frequency. Over the course of 24 hours, we achieve an absolute temperature stability within 50 mK and a relative amplitude stability of 100 kHz/72.9 MHz $\approx 10^{-3}$, suggesting that we have a relative amplitude sensitivity of 1% per 500 mK. We note that the timescale for a typical calibration and measurement of a dataset presented in this paper is roughly a few hours, meaning we can operate in a window where the relative amplitude stability can be much better than 10^{-3} .

APPENDIX D: CALIBRATION PROCEDURES

In this appendix, we describe the various calibration experiments in detail along with their pulse sequences.

1. Tomography of the Rabi qubit

We initialize eigenstates $|\pm\rangle$ of $\hat{\sigma}_x$ in the driven frame by first preparing the corresponding states of the undriven

transmon via a standard $\pi/2$ rotation and then adiabatically ramping on the Rabi drive $\tau^R_{\rm ramp}\gg 1/\Delta_R$. In order to measure the Rabi qubit in the driven basis, we need a decoding operation that maps the driven states $|\pm\rangle$ onto our measurement basis $|g/e\rangle$. Given that our decoding operation is a $\pi/2$ rotation performed using the same microwave clock as the initial $\pi/2$ rotation, we need to know the phase evolution of the $|\pm\rangle$ states in the frame of this drive centered at the bare g-e transition frequency ω_q of the transmon. Notably, this phase depends on the Rabi frequency Ω_R , the static detuning Δ_R , the evolution time τ , and a fixed offset phase φ_0 :

$$\varphi_{\text{decode}} = (\Omega_R - \Delta_R)\tau + \varphi_0.$$
(D1)

By calibrating this rate appropriately, we are able to continuously measure $\langle \hat{\sigma}_x \rangle$ as a function of time and extract a corresponding driven coherence time (see Fig. 8) [34]. In all of the experiments in this paper, we choose to map $|+\rangle \rightarrow |e\rangle$ and $|-\rangle \rightarrow |g\rangle$. As such, we have the mapping $\langle \hat{\sigma}_x \rangle = 2\langle \hat{P}_e \rangle - 1$.

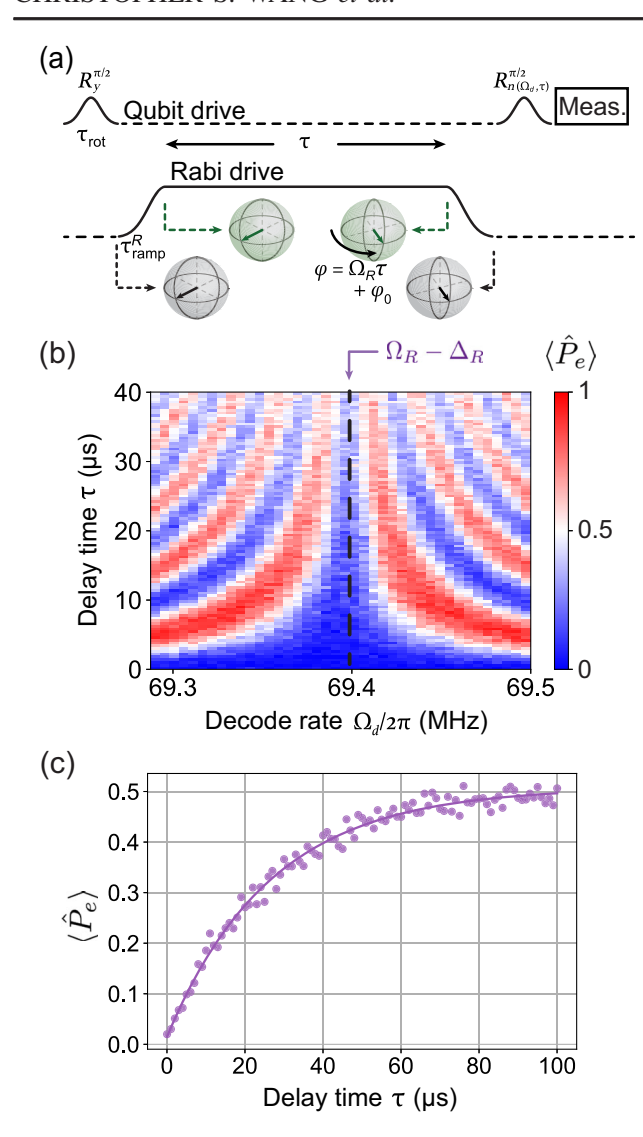


FIG. 8. Free evolution of the driven Rabi qubit. (a) A Ramsey-style pulse sequence is used to calibrate the decode rate. The final $\pi/2$ rotation has a phase that depends on both the delay time τ and the programmed decode rate Ω_d . (b) The 2D plot reveals an optimal decode rate which is inferred to be equal to the true Rabi frequency offset by the static detuning $\Omega_R - \Delta_R$. (c) The decode rate can then be fixed to the optimal value to extract a driven transverse relaxation time $T_{2\rho} \approx 27$ µs via fitting to an exponential decay function (solid line).

2. Individual sideband interactions

The sideband interactions have the form:

$$\hat{H}_{\text{red}}/\hbar = g\hat{c}\hat{\sigma}_z^- + g^*\hat{c}^{\dagger}\hat{\sigma}_z^+, \tag{D2}$$

$$\hat{H}_{\rm blue}/\hbar = g\hat{c}\hat{\sigma}_z^+ + g^*\hat{c}^\dagger\hat{\sigma}_z^-, \tag{D3}$$

for a general cavity annihilation operator \hat{c} , and $\hat{\sigma}_z^{+(-)} = |\tilde{e}(\tilde{g})\rangle\langle\tilde{g}(\tilde{e})|$ are the raising and lowering operators of the two driven qubit eigenstates that adiabatically connect to the ground and first excited state of the transmon. For our

system, we have $\hat{c} \in \{\hat{a}, \hat{b}\}$. The qualitative behavior of each individual sideband interacting with the driven qubit will be different given that we are operating in the regime where $g > \kappa_a$ and $g \lesssim \kappa_b$. The former will result in either creating and annihilating two excitations simultaneously $|\tilde{g},0\rangle \leftrightarrow |\tilde{e},1\rangle$ (red sideband) or a coherent exchange between an excitation in the driven qubit and a photon in the cavity $|\tilde{e},0\rangle \leftrightarrow |\tilde{g},1\rangle$ (blue sideband) [51]. The latter will stabilize the qubit in either the excited state $|\tilde{e}\rangle$ (red sideband) or the ground state $|\tilde{g}\rangle$ (blue sideband) [52]. To solidify the connection with these previous experiments, we note that $|\tilde{g}\rangle \approx (1/\sqrt{2})(|g\rangle + |e\rangle)$ and $|\tilde{e}\rangle \approx (1/\sqrt{2})(|g\rangle - |e\rangle)$ when expressed in the basis of undriven transmon eigenstates.

In order to calibrate the interaction strengths, we will operate in the restricted two-dimensional subspace of the joint Hilbert space of the cavity and qubit as described above. This allows us to simplify our analysis and replace the qubit raising and lowering operators $\hat{\sigma}_z^{\pm}$ with general bosonic creation and annihilation operators $\hat{d}^{(\dagger)}$. We then follow Refs. [47,53] and capture the full range of dynamics by solving the equations of motion for \hat{d} under \hat{H}_{blue} and incorporating a cavity damping rate κ . We also include a static detuning term $\delta \hat{c}^{\dagger} \hat{c}$ to capture the effect of sweeping the pump frequency that enables the interaction. The resulting field has the form:

$$\hat{d}(t) = \frac{\hat{d}(0)}{\Omega} e^{-\kappa_{\text{eff}} t/4} \left[\Omega \cosh\left(\frac{\Omega t}{4}\right) + \kappa_{\text{eff}} \sinh\left(\frac{\Omega t}{4}\right) \right], \tag{D4}$$

where
$$\Omega = \sqrt{\kappa_{\rm eff}^2 - (4g)^2}$$
 and $\kappa_{\rm eff} = \kappa + 2i\delta$.

For each interaction, we prepare our system in either $|\tilde{e},0\rangle$ (blue sidebands) or $|\tilde{g},0\rangle$ (red sidebands) and scan the frequency of the cavity sideband and the delay time for a given pump amplitude. By measuring the qubit population, we extract $\langle \hat{d}^{\dagger}(t)\hat{d}(t)\rangle$ and can fit the resulting data using Eq. (D4). For the exchange interaction under the blue sideband, we have $\langle \hat{d}^{\dagger}(0)\hat{d}(0)\rangle_{\rm blue}=1$ for the qubit initially in its excited state, giving us an expression for $\langle \hat{d}^{\dagger}(t)\hat{d}(t)\rangle_{\text{blue}}$. For the red sideband, the features are qualitatively identical, with the exception that the qubit starts out in the ground state, giving us $\langle \hat{d}^{\dagger}(t)\hat{d}(t)\rangle_{\mathrm{red}}=$ $1 - \langle \hat{d}^{\dagger}(t)\hat{d}(t)\rangle_{\text{blue}}$. Notably, this assumes that the effective interaction strength g is independent of the pump detuning δ , which is strictly not true but should be a very good approximation in our regime given that the scale of the chevron features, set by g, is much smaller than the absolute detuning from the cavity resonance $\sim \Omega_R$. We allow for an overall amplitude, global offset, and time offset in our fit, leaving g and κ to be the only free parameters. In the case of the coupling mode, we first perform this fit for a range of interaction strengths $g \approx \kappa_b$

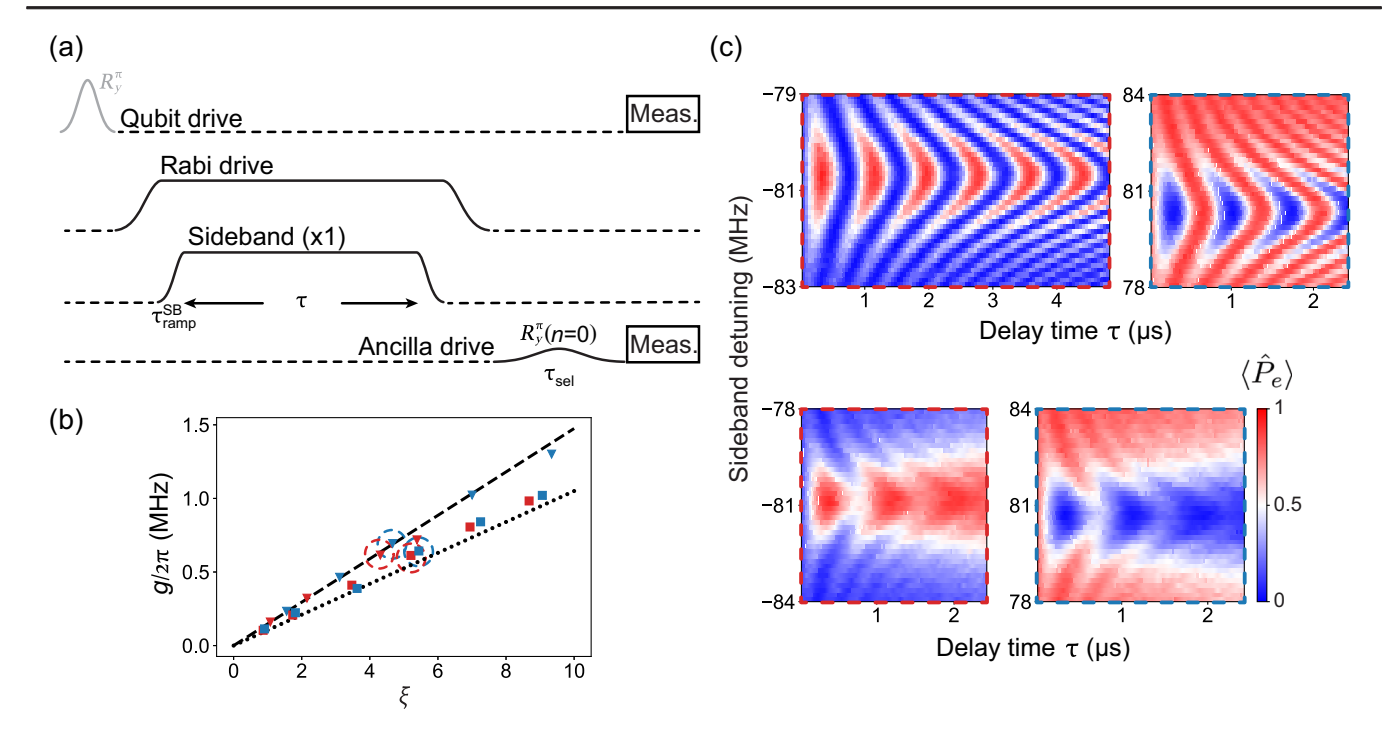


FIG. 9. Calibrating individual exchange interactions. (a) Pulse sequence. The transmon is initialized in either $|g\rangle$ or flipped to $|e\rangle$ with a π rotation depending on if the red or blue sideband is activated. The sideband is turned on with a ramp time $\tau_{\text{ramp}}^{\text{SB}} \gg 1/\Delta_{\text{SB}}$, where $\Delta_{\text{SB}} = \omega_{\text{pump}} - \omega_c$ is the detuning from the sideband to the Stark-shifted cavity frequency. A frequency selective π rotation of the ancilla qubit maps the vacuum projector of the tuning mode onto the state of the ancilla, which is subsequently measured with the qubit simultaneously. (b) Interaction strengths g for individual sideband interactions between the driven qubit and the tuning mode (triangles) or coupling mode (squares). g is extracted via a fit using Eq. (D4) for the red sidebands (red markers) and blue sidebands (blue markers). Error bars are smaller than the markers. ξ is calibrated via independent measurements of $\chi_{a/b}$ and the qubit's Stark shift as a function of pump amplitude. Dashed and dotted lines represent the expected interaction strength in the ideal case $g = \chi_{a/b} \xi/2$ for the tuning and coupling modes, respectively. Deviations of the data from a linear relation for the tuning mode coincides with regions where the Stark shift becomes nonlinear in pump power. Slight disagreement between the data and theory expectation for the coupling mode may stem from an inaccurate estimate of χ_b and from a sensitivity of the extracted fit values to a true value of κ_b . (c) Raw calibration data of the qubit population for a fixed pump amplitude [dashed circles in (b)] for the tuning mode (top) and coupling mode (bottom). The sideband detunings are referenced to the cavity frequencies, showing that we are operating at Rabi frequencies $\Omega_R/2\pi \approx 80$ MHz.

and extract a decay rate $\kappa_b/2\pi \approx 320$ kHz. For the remainder of the calibrations where $g < \kappa_b$, we fix this quantity and let the interaction strength g be the only free parameter to be fitted. The full calibration for different pump amplitudes is shown in Fig. 9.

3. Conditional displacements

The combination of simultaneous red and blue cavity sidebands enacts a conditional displacement interaction. This requires that two conditions are fulfilled: (1) the interaction strengths of each individual sideband interaction be equal and (2) the frequency difference between the two sidebands equals twice the Rabi frequency. If these two conditions are met, then we can model the interaction using Eq. (B12).

In practice, the presence of each sideband will Stark shift both the transmon and cavity modes. Thus, to capture the dominant effect of all of these Stark shifts (which influences the resonance condition), we perform individual sideband calibrations with the opposite sideband on but detuned by an amount larger than the interaction strength we are using (i.e., by an additional 2 MHz in our experiments). We scan the pump amplitudes and match the individual sideband strengths before bringing both sidebands into resonance. This relies on the assumption that over a variation of ~2 MHz, the relative change in the cavity Stark shift, which influences the dimensionless pump strength that determines the interaction strength, is negligible. Finally, we fine-tune the difference frequency of the two sidebands while keeping the average value fixed [which fixes Δ_c in Eq. (B12) in order to account for any change in the Rabi frequency which we are very sensitive to]. This sensitivity is revealed by measuring the transverse relaxation time $T_{2\rho}$, and choosing a calibration point where this value is maximized, suggesting that the resonance conditions are fulfilled as well as possible. This calibration procedure gives us the data shown in Fig. 2(b) of the main text.

For the tuning mode, the dynamics of an initial vacuum state $|\alpha_0=0\rangle_a$ evolving under a conditional displacement

interaction will be a circular trajectory in phase space around the location of the ground state $\alpha_g = g_x/\Delta_a$. By measuring the population in $|n=0\rangle_a$, we are effectively measuring the overlap of a coherent state with itself as it oscillates in time. This justifies the use of a simple model, where the state autocorrelation function is $\langle \beta e^{-i\Delta t} | \beta \rangle = e^{|\beta|^2(e^{-i\Delta_a t}-1)}$. The corresponding probability is

$$P_0 = |\langle \beta e^{-i\Delta_a t} | \beta \rangle|^2 = e^{2|\beta|^2 (\cos[\Delta_a t] - 1)}.$$
 (D5)

To make the connection with our model, we choose $\beta = \alpha_g = g_x/\Delta_a$. We use Eq. (D5) (along with an overall amplitude and offset to account for preparation and measurement errors) as our fitting function for the data in Fig. 2(b) of the main text.

4. Cavity displacements along the interaction axis

As described in Appendix B, the cavity phase of the conditional displacement [i.e., the phase which defines the position operator $\hat{x} \propto (\hat{c}e^{i\varphi_{\Sigma}} + \hat{c}^{\dagger}e^{-i\varphi_{\Sigma}})$] is determined by the sum phase of the red and blue sidebands. Given that we are turning on the conditional displacement interaction suddenly ($\tau_{\rm ramp}^{\rm SB} \ll 1/g$), the phase of our initial displacement operation $\hat{\mathcal{D}}(\alpha_0)$ on the tuning mode will determine the location in the driven phase space where the wave packet begins. Displacements whose phase is aligned to the conditional displacement cavity phase will prepare wave packets along the position axis, whereas care needs to be taken to prepare wave packets with various momentums that are located at one of the two ground state positions. In

our experiment, we prepare coherent states with no initial momentum along the reaction coordinate.

In order to calibrate the displacement phase, we begin with a calibrated conditional displacement where we have extracted g_x and Δ_a , which gives us a value for the ground state amplitude $\alpha_g = g_x/\Delta_a$ [Fig. 2(b) of the main text]. Note that this does not rely on any displacement phase since we are starting off in a vacuum state. Next, we scan the phase of an initial displacement of $2\alpha_q$ and turn on the conditional displacement interaction for various delay times. The optimal phase will be the one where we recover revivals that are half a period out of phase from those in Fig. 2(b) of the main text. This can be interpreted as follows. A vacuum state in the lab frame $|0\rangle_{lab}$ looks like a displaced state $|-\alpha_g\rangle_{\rm disp}$ with respect to the displaced ground state $|lpha_g
angle_{
m lab}=|0
angle_{
m disp}$, and thus will oscillate around the ground state, reaching $|\alpha_q\rangle_{\text{disp}}$ after half a period. By determining the phase that enables us to prepare $|lpha_g
angle_{
m disp}$ (which is $|2\alpha_q\rangle_{lab}$ in the lab frame and will return to the vacuum state $|-\alpha_g\rangle_{\mathrm{disp}}$ after half a period), we can prepare any state along the position axis, including the displaced ground state, as shown in Fig. 10(b).

5. Echoing the residual entanglement during ramping of the Rabi drive

The adiabatic preparation of our driven qubit eigenstates as motivated in Appendix B 2 has two benefits: for a fixed transmon anharmonicity, we can (1) use larger Rabi frequencies while canceling the residual cross-Kerr and (2) avoid leakage events to higher transmon levels (up to

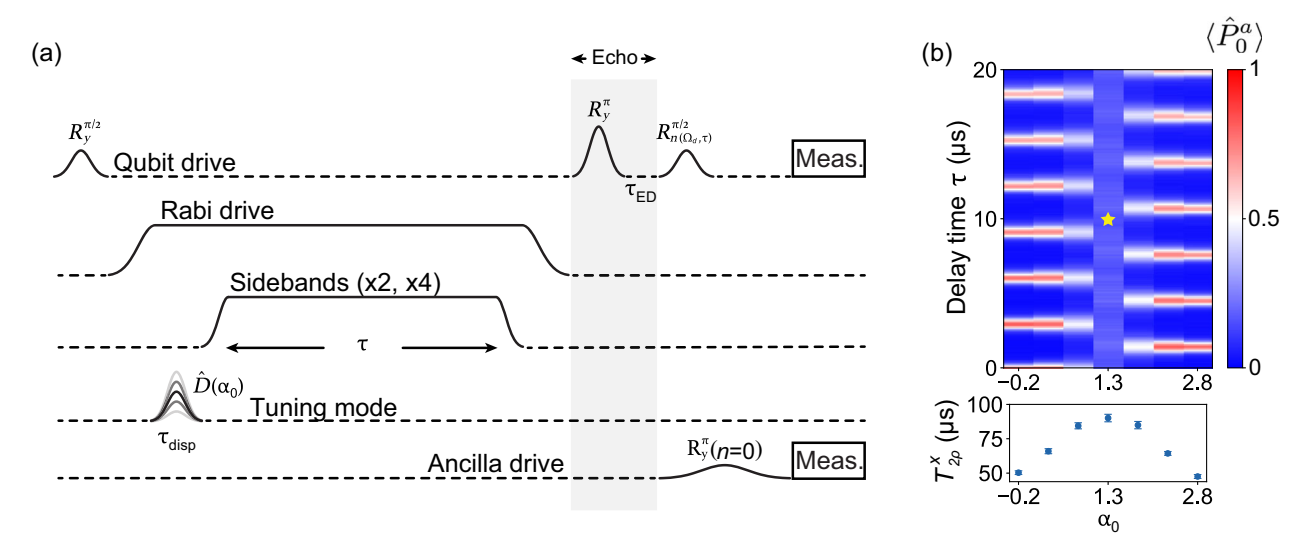


FIG. 10. Calibrating conditional displacements. (a) Pulse sequence. The displacement pulse is played after the Rabi drive is turned on and the cross-Kerr is nulled. An echo sequence eliminates the residual entanglement between the qubit and cavity during the ramp off of the Rabi drive. (b) Top: coherent revivals for various initial displacements along the interaction axis, probed through measurement of the vacuum projector. The contrast is maximized when the wave packet passes through the origin, and oscillations vanish when the ground state $\alpha_g \approx 1.3$ is prepared. The data in Fig. 3(b) are taken at the location of the yellow star. Bottom: simultaneous measurement of $T_{2\rho}^x$ reveals driven coherence times with a slight dependence on $\langle \hat{a}^{\dagger} \hat{a} \rangle$.

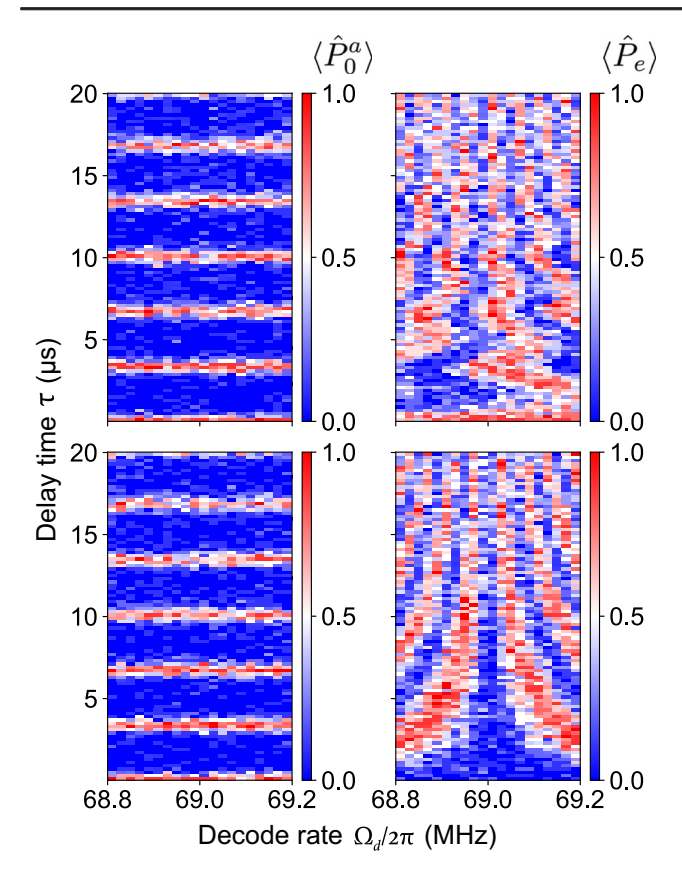


FIG. 11. Echoing away residual entanglement. Simultaneous measurement of the vacuum projector on the tuning mode via a transmon ancilla (left) and the driven qubit (right) while \hat{H}_a is active. The pulse sequence used for this calibration is shown in Fig. 10 without (top) and with (bottom) the π rotation and echo delay $\tau_{\rm ED}$ and only sidebands on the tuning mode. There is no initial displacement amplitude ($\alpha_0=0$). Time dynamics of the tuning mode's vacuum projector reveals coherent revivals as expected [as in Fig. 2(c) of the main text], independent of the decode rate on the driven qubit. Scanning the decode rate without the echo sequence results in distortions to the driven Ramsey data that are correlated with the cavity photon distribution. Implementing the echo sequence eliminates this effect, suggesting that the systems remain unentangled at all delay times. Here, we use an optimized value of the delay time $\tau_{\rm ED}=144$ ns.

natural heating rates of the dressed eigenstates) associated with a resonant drive. The primary consequence of this approach is the undesired interaction between the qubit and cavity photons during the ramp time of the Rabi drive.

Qualitatively, this undesired interaction stems from ramping between the static interaction Hamiltonian $\hat{H}_{\rm int}/\hbar = -\chi \hat{c}^{\dagger} \hat{c} \hat{q}^{\dagger} \hat{q}$ and the driven Hamiltonian where the cross-Kerr interaction is nulled. Thus, if there are photons in the cavity during either the ramp on or off of the Rabi drive, they will entangle with the superposition states of the qubit that we are manipulating. We can avoid this effect during the ramp on of the Rabi drive by performing our displacement operation after the Rabi drive

is fully ramped on, i.e., during the time when the cross-Kerr interaction is nulled [see Fig. 10(a)]. For addressing the entanglement during the ramp off of the Rabi drive, we implement a simple and short echo sequence of the qubit to undo the interaction. This works because the entanglement is fully determined by χ and the ramp time τ_{ramp}^R and not the cavity photon distribution. This is important as we do not want a scheme which depends on the cavity state that we are manipulating. Figure 11 shows how implementing this protocol eliminates spurious features that arise from this entanglement when performing a decode calibration experiment [Fig. 8(b)] when \hat{H}_a is active. In practice, this calibration is only done with respect to photons in the tuning mode. Given that we operate the coupling mode in a regime where $g_{v} < \kappa_{b}$, the photon distribution remains relatively small and thus any residual entanglement effects are negligible.

APPENDIX E: EXTENDED DATA AND POSTSELECTING ON LEAKAGE EVENTS

In this appendix, we present additional data (Fig. 12) that support what is shown in the main text, specifically focusing on leakage statistics. Our measurement of the transmon is able to distinguish between $\{|g\rangle, |e\rangle, |f\rangle\}$ on a single-shot basis, which gives us information on leakage events outside the qubit manifold that we use for our experiments. In the absence of decoherence, our adiabatic preparation scheme should ideally eliminate any leakage to the second excited state $|f\rangle$ and higher (assuming there are no accidental resonances induced by the drives). In practice, any relaxation or heating between undriven transmon levels will lead to transitions between the driven eigenstates that have finite support across multiple undriven basis states. In all of the data presented, we postselect away outcomes where the transmon is measured to be in $|f\rangle$. We compile the postselection statistics in Table II, and note that overall the leakage probabilities are small.

APPENDIX F: MASTER EQUATION SIMULATIONS

The theoretical predictions for $\langle \hat{\sigma}_x \rangle$ in Figs. 2(d) and 4(b) are obtained by performing a numerical simulation of a full time-domain master equation using a PYTHON-based open source software (QuTiP):

$$\dot{\hat{\rho}} = -\frac{i}{\hbar}[\hat{H}_{\text{sim}}, \hat{\rho}] + \kappa_b \mathcal{D}[\hat{b}]\hat{\rho} + \frac{\gamma_y}{2} \mathcal{D}[\hat{\sigma}_y]\hat{\rho},$$

where the left-hand side of the equation is the time derivative of the system's density matrix and $\mathcal{D}[\hat{A}]\hat{\rho}=\hat{A}\,\hat{\rho}\,\hat{A}^{\dagger}-\frac{1}{2}\hat{A}^{\dagger}\hat{A}\,\hat{\rho}-\frac{1}{2}\hat{\rho}\hat{A}^{\dagger}\hat{A}$. We extract $\langle\hat{\sigma}_{x}\rangle$ by plotting $\text{Tr}[\hat{\rho}^{\text{qubit}}\hat{\sigma}_{x}]$, where $\hat{\rho}^{\text{qubit}}=\text{Tr}_{a,b}\hat{\rho}$ is the reduced density matrix of the qubit only. For the measurement-induced

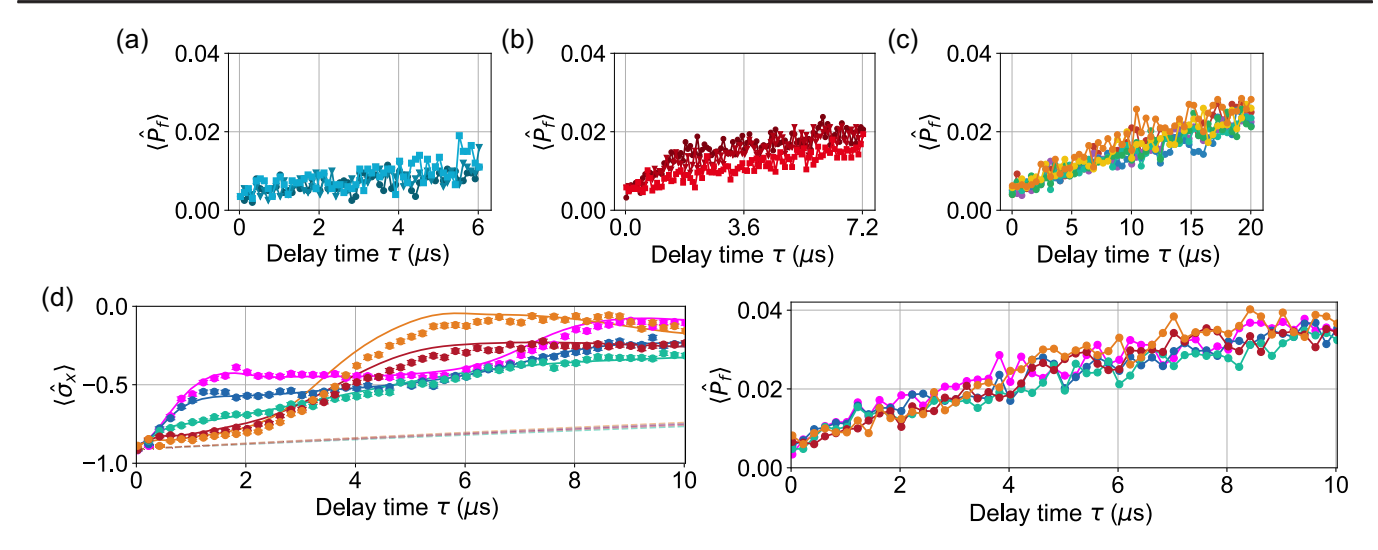


FIG. 12. Extended data and leakage statistics. (a)–(c) Probability of leaking out of the qubit subspace to $|f\rangle$ for the data presented in Figs. 2(b), 2(c), and 10, respectively. (d) The same dataset as appears in Fig. 4(a) (left), but including two additional initial states with $|\alpha_0\rangle_a = |\alpha_g/2\rangle_a$ (blue) and $|3\alpha_g/2\rangle_a$ (red), with the associated leakage probabilities (right). All of the leakage probabilities are equivalent to the percentage of data that is postselected away for the rest of the data in the paper, which is always less than 5%.

dephasing in Fig. 2(d), we use $\hat{H}_{\rm sim} = \hat{H}_b$ from Eq. (2) and an initial state $|-\rangle \otimes |0\rangle_b$ for various values of Δ_b . For the full system dynamics through the conical intersection in Fig. 4(b), we use $\hat{H}_{\rm sim} = \hat{H}_{\rm LVC}$ from Eq. (3) and initial states $|-\rangle \otimes |\alpha_0\rangle_a \otimes |0\rangle_b$ for various values of α_0 .

Across these two simulations, the parameters $\{g_x, \Delta_a, g_y, \kappa_b\}$ are determined via independent calibrations, and Δ_b is estimated via the frequencies of the sidebands on the coupling mode. The value of γ_y is set by an independent measurement of $T_{2\rho}^x$, specifically via $\gamma_y = 1/T_{2\rho}^x$. Finally, the amplitude and offset are adjusted using the measured experimental values from the

corresponding $T_{2\rho}^x$ control measurement, leaving zero free parameters.

APPENDIX G: DISSIPATION ANALYSIS AND ZENO DYNAMICS

In this appendix, we describe the oscillator-induced dissipation of the qubit resulting from the evolution under the master equation,

$$\dot{\hat{\rho}} = -\frac{i}{\hbar} [\hat{H}_{\text{Zeno}}, \hat{\rho}] + \kappa_b \left(\hat{b} \,\hat{\rho} \,\hat{b}^{\dagger} - \frac{1}{2} \hat{b}^{\dagger} \hat{b} \,\hat{\rho} - \frac{1}{2} \hat{\rho} \hat{b}^{\dagger} \hat{b} \right), \quad (G1)$$

TABLE II. Extended data information. Quantities in brackets correspond to identifiers within a dataset. Different values of Δ_c , $c \in \{a, b\}$, require a fine-tuning calibration on the drive configuration to match Rabi frequency shifts, but preparing different initial states does not.

Dataset	Drives (+Rabi)	Figures	$\Omega_R[\Delta_c]/2\pi$ (MHz)	$T_{2\rho} [\alpha_0] (\mu s)$	Leakage
Coherent state revivals	Tuning mode sidebands	2(a)	82.532 [0.457] 82.532 [0.355]	Not measured	Fig. 12(a)
	runnig mode sidebands	2(c)	82.492 [0.246]	Not illeasured	11g. 12(a)
Measurement-induced dephasing	Coupling mode sidebands	2(d)	79.915 [0]	36.6	
			79.9175 [0.4]	40.5	Fig. 12(b)
			79.9225 [0.8]	36.3	
Coherent revivals + state preparation	Tuning and coupling mode sidebands	10(b)	80.045	see Fig. 10(b)	Fig. 12(c)
Conical intersection dynamics				51.7 [0]	
				51.1 $[\alpha_q/2]$	
	Tuning and coupling mode sidebands	4(a)	81.013	57.8 $\left[\alpha_{g}\right]$	Fig. 12(d)
				53.9 $[3\alpha_g/2]$	
				48.8 [$2\alpha_g$]	

with

$$\hat{H}_{\text{Zeno}}/\hbar = E(x)\hat{\sigma}_x + \Delta_b \hat{b}^{\dagger} \hat{b} + g\hat{\sigma}_z(\hat{b}^{\dagger} + \hat{b}) \quad (G2)$$

from Eq. (5) of the main text. The dynamics of the system are effectively the same as Zeno dynamics of a driven qubit generated by the competition between $E(x)\hat{\sigma}_x$, which tries to lock the state of the qubit to an eigenstate of $\hat{\sigma}_x$, and $g\hat{\sigma}_z(\hat{b}^\dagger+\hat{b})$, which in combination with photon loss in the oscillator tries to project the state of the qubit onto an eigenstate of $\hat{\sigma}_z$. Note that here we choose the dissipation to be along $\hat{\sigma}_z$ as opposed to $\hat{\sigma}_y$. The resulting dissipative dynamics is crucially dependent on the parameters E(x), Δ_b , g, κ_b . While an exact analytic expression for the time dependence of the qubit density matrix cannot be obtained in general, here we consider a few extreme parameter regimes which can be easily analyzed and provide a window to the vast range of qubit dynamics possible.

This simplest case is when E(x) = 0. In this case, it is possible to use Fokker-Planck equations to calculate an effective dephasing rate. However, when $E(x) \neq 0$, this approach will fail to give an analytical expression for the dephasing rate. In this case, we will invoke additional constraints which will allow us to apply the Born-Markov approximation and derive an effective master equation for the qubit.

1.
$$E(x) \neq 0$$

To get a simple intuitive understanding of the oscillator-induced dephasing when $E(x) \neq 0$, we consider two cases: (a) $\Delta_b = 0$, $\kappa_b \gg g$ and (b) $|2\Delta_b - E(x)| \ll |2\Delta_b + E(x)|$, $|2\Delta_b + E(x)| \gg \kappa_b \gg |2\Delta_b - E(x)|$, g.

Case (a)—In this case, the oscillator mode can be eliminated using the standard Born-Markov approximation and a simple effective master equation for the qubit is obtained:

$$\hat{\rho}_q = -i[\hat{H}_q, \hat{\rho}_q] + \kappa_q(\hat{\sigma}_z \hat{\rho}_q \hat{\sigma}_z - \hat{\rho}_q), \tag{G3}$$

with $\hat{H}_q = E(x)\hat{\sigma}_x$, $\kappa_q = g^2\kappa_b/[4E(x)^2 + \kappa_b^2/4]$. Note that we have set $\hbar=1$ and will do so from here onwards. In this case, the state of the qubit will be an equal mixture of $|+\rangle$ and $|-\rangle$ or $|g\rangle$ and $|e\rangle$.

Case (b)—In this case, the standard Born-Markov approximation yields the following master equation:

$$\begin{split} \hat{\rho}_{q} &= -i[\hat{H}_{q},\hat{\rho}_{q}] \\ &+ \kappa_{q} \bigg(|-\rangle \langle +|\hat{\rho}_{q}|+\rangle \langle -|-\frac{1}{2}|+\rangle \langle +|\hat{\rho}_{q}-\frac{1}{2}\hat{\rho}_{q}|+\rangle \langle +| \bigg), \end{split} \tag{G4}$$

with $\hat{H}_q = E(x)\hat{\sigma}_x$, $\kappa_q = g^2\kappa_b/\{[2E(x) - \Delta_b]^2 + \kappa_b^2/4\}$. Unlike in case (a), here, the steady state of the qubit will

be the pure state $|+\rangle$. The difference between the master equations Eqs. (G3) and (G4) can be understood by observing that when $|2\Delta_b + E(x)| \gg \kappa_b \gg |2\Delta_b - E(x)|$, then the transition between $|+\rangle \otimes |0\rangle$ and $|-\rangle \otimes |1\rangle$ becomes more likely than that between $|+\rangle \otimes |1\rangle$ to $|-\rangle \otimes |0\rangle$ because the former, happening at frequency $2\Delta_b - E(x)$, lies within the bandwidth κ_b . The first term in the tensor product refers to the state of the qubit and the second term refers to the vacuum $|0\rangle$ and single photon Fock state $|1\rangle$ of the oscillator mode. Consequently, if the photon is subsequently lost from the oscillator, the qubit will be preferentially projected to the state $|-\rangle$.

Thus, the steady-state value of $\langle \hat{\sigma}_x \rangle$ is 0 for case (a) and -1 for case (b). Clearly, we see that the qubit dynamics depends on the parameters $\{E(x), \Delta_b, g, \kappa_b\}$, and in certain cases can have a steady-state value of $\langle \hat{\sigma}_x \rangle$ between 0 and -1.

We note here that by considering our full model [Eq. (3) of the main text] with not only dissipation on the coupling mode κ_b but also dissipation on the tuning mode κ_a , we can expect a more complex landscape of steady-state dynamics which may qualitatively fall into the above regime.

2.
$$E(x) = 0$$

In this case, we follow the approach in Ref. [41] and begin by writing the density matrix of the qubit and oscillator as

$$\hat{\rho} = |g\rangle\langle g| \otimes \hat{\rho}_{gg} + |e\rangle\langle e| \otimes \hat{\rho}_{ee} + |g\rangle$$

$$\times \langle e| \otimes \hat{\rho}_{ge} + |e\rangle\langle g| \otimes \hat{\rho}_{eg}, \tag{G5}$$

where $|g,e\rangle$ represent the qubit states and $\hat{\rho}_{ij}$ acts on the oscillator Hilbert space conditioned on the qubit state. From Eqs. (G1) and (G2) with E(x)=0 and Eq. (G5), we get

$$\dot{\hat{\rho}}_{ge} = -ig(\hat{b}^{\dagger} + \hat{b})\hat{\rho}_{ge} - ig\hat{\rho}_{ge}(\hat{b}^{\dagger} + \hat{b})
- i\Delta_{b}(\hat{b}^{\dagger}\hat{b}\hat{\rho}_{ge} - \hat{\rho}_{ge}\hat{b}^{\dagger}\hat{b}) + \kappa_{b}\hat{b}\hat{\rho}_{ge}\hat{b}^{\dagger}
- \frac{\kappa_{b}}{2}\hat{b}^{\dagger}\hat{b}\hat{\rho}_{ge} - \frac{\kappa_{b}}{2}\hat{\rho}_{ge}\hat{b}^{\dagger}\hat{b}.$$
(G6)

Next, we use the positive-P representation $\hat{\rho}_{ge} = \int P(\alpha, \alpha^*, t) d\alpha d\alpha^*$ and write the effective Fokker-Planck equation:

$$\frac{\partial P}{\partial t} = -2igP(\alpha + \alpha^*) + i(g + \Delta_b \alpha) \frac{\partial P}{\partial \alpha}
+ i(g - \Delta_b \alpha^*) \frac{\partial P}{\partial \alpha^*} + \kappa_b P + \frac{\kappa_b \alpha}{2} \frac{\partial P}{\partial \alpha}
+ \frac{\kappa_b \alpha^*}{2} \frac{\partial P}{\partial \alpha^*}.$$
(G7)

Now we must solve the above equation with some given initial condition. In the setup of interest we start with the

oscillator mode in vacuum so that $P(\alpha, \alpha^*, 0) = \delta^2(\alpha) = \lim_{\epsilon \to 0} (1/\pi\epsilon) \exp(-|\alpha|^2/\epsilon)$ and the qubit in the state $|+\rangle$. We can make the Gaussian ansatz, $P(\alpha, \alpha^*, t) = \exp[-a(t) + b(t)\alpha + c(t)\alpha^* - d(t)|\alpha|^2]$ and write the equivalent differential equations for a, b, c, d to get

$$\begin{split} -\dot{a} &= igb + igc + \kappa_b, \\ -\dot{d} &= -\kappa_b d, \\ \dot{b} &= -2ig + \left(i\Delta_b + \frac{\kappa_b}{2}\right)b - igd, \\ \dot{c} &= -2ig + \left(-i\Delta_b + \frac{\kappa_b}{2}\right)b - igd. \end{split} \tag{G8}$$

These time-dependent equations can be easily solved with initial conditions now written as $a(0) = \ln \pi \varepsilon$, b(0) = 0, c(0) = 0, $d(0) = 1/\varepsilon$, but the analytic expressions are considerably simplified when $\Delta_b = 0$. Once we get a, b, c, d we are able to reconstruct P and hence $\hat{\rho}_{ge}$. The relevant quantity of interest is the time dependence of the expectation value of the operator $|g\rangle\langle e|$:

$$\langle |g\rangle\langle e|(t)\rangle = \text{Tr}[\hat{\rho}_{ge}] = \int P(\alpha, \alpha^*, t)d^2\alpha.$$
 (G9)

For $\Delta_b = 0$ and an initial condition where the qubit is in $|+\rangle$ and the oscillator in vacuum, we have

$$\langle |g\rangle\langle e|(t)\rangle = \frac{1}{2}\exp\left[-\frac{8g^2t}{\kappa_b} + \frac{16g^2}{\kappa_b^2}(1 - e^{-\kappa_b t/2})\right]. \quad (G10)$$

Next, we consider the rate equation for $\hat{\rho}_{gg}$:

$$\begin{split} \dot{\hat{\rho}}_{gg} &= -ig(\hat{b}^{\dagger} + \hat{b})\hat{\rho}_{gg} + ig\hat{\rho}_{gg}(\hat{b}^{\dagger} + \hat{b}) \\ &- i\Delta_{b}(\hat{b}^{\dagger}\hat{b}\hat{\rho}_{gg} - \hat{\rho}_{gg}\hat{b}^{\dagger}\hat{b}) + \kappa_{b}\hat{b}\hat{\rho}_{gg}\hat{b}^{\dagger} - \frac{\kappa_{b}}{2}\hat{b}^{\dagger}\hat{b}\hat{\rho}_{gg} \\ &- \frac{\kappa_{b}}{2}\hat{\rho}_{gg}\hat{b}^{\dagger}\hat{b}. \end{split} \tag{G11}$$

Like before, we use the positive-P representation $\hat{\rho}_{qq} = \int P(\alpha, \alpha^*, t) d\alpha d\alpha^*$, so that

$$\begin{split} \frac{\partial P}{\partial t} &= -ig\frac{\partial P}{\partial \alpha^*} + ig\frac{\partial P}{\partial \alpha} - i\Delta_b \frac{\partial \alpha^* P}{\partial \alpha^*} + i\Delta_b \frac{\partial \alpha P}{\partial \alpha} \\ &\quad + \frac{\kappa_b \alpha}{2} \frac{\partial P}{\partial \alpha} + \frac{\kappa_b \alpha^*}{2} \frac{\partial P}{\partial \alpha^*}. \end{split} \tag{G12}$$

We can again make the Gaussian ansatz $P(\alpha, \alpha^*, t) = \exp[-a(t) + b(t)\alpha + c(t)\alpha^* - d(t)|\alpha|^2]$, and solve the corresponding differential equations for a, b, c, d to get $P(\alpha, \alpha^*, t) = \delta^2[\alpha - \alpha(t)]$, where $\alpha(t) = 2ig[1 - \exp(-\kappa_b t/2)]/\kappa_b$ (for $\Delta_b = 0$). Thus, $\langle |g\rangle\langle g|(t)\rangle = 1/2$. Similarly we can show that $\langle |e\rangle\langle e|(t)\rangle = 1/2$. Hence the diagonal terms of the qubit density matrix do not decay

with time—only the off-diagonal terms do. Thus, in this case the qubit undergoes pure dephasing due to its coupling with the oscillator mode and at steady state becomes an equal mixture of $|g\rangle$ and $|e\rangle$.

- [1] A. Aspuru-Guzik, A. D. Dutoi, P. J. Love, and M. Head-Gordon, *Simulated Quantum Computation of Molecular Energies*, Science **309**, 1704 (2005).
- [2] A. Peruzzo, J. McClean, P. Shadbolt, M.-H. Yung, X.-Q. Zhou, P. J. Love, A. Aspuru-Guzik, and J. L. O'Brien, A Variational Eigenvalue Solver on a Photonic Quantum Processor, Nat. Commun. 5, 4213 (2014).
- [3] A. Kandala, A. Mezzacapo, K. Temme, M. Takita, M. Brink, J. M. Chow, and J. M. Gambetta, *Hardware-Efficient Variational Quantum Eigensolver for Small Molecules and Quantum Magnets*, Nature (London) **549**, 242 (2017).
- [4] A. Potočnik, A. Bargerbos, F. A. Y. N. Schröder, S. A. Khan, M. C. Collodo, S. Gasparinetti, Y. Salathé, C. Creatore, C. Eichler, H. E. Türeci, A. W. Chin, and A. Wallraff, Studying Light-Harvesting Models with Superconducting Circuits, Nat. Commun. 9, 904 (2018).
- [5] C. Maier, T. Brydges, P. Jurcevic, N. Trautmann, C. Hempel, B. P. Lanyon, P. Hauke, R. Blatt, and C. F. Roos, *Environ-ment-Assisted Quantum Transport in a 10-Qubit Network*, Phys. Rev. Lett. **122**, 050501 (2019).
- [6] C. Sparrow, E. Martín-López, N. Maraviglia, A. Neville, C. Harrold, J. Carolan, Y. N. Joglekar, T. Hashimoto, N. Matsuda, J. L. O'Brien, D. P. Tew, and A. Laing, Simulating the Vibrational Quantum Dynamics of Molecules Using Photonics, Nature (London) 557, 660 (2018).
- [7] J. Huh, G. G. Guerreschi, B. Peropadre, J. R. McClean, and A. Aspuru-Guzik, *Boson Sampling for Molecular Vibronic Spectra*, Nat. Photonics 9, 615 (2015).
- [8] C. S. Wang, J. C. Curtis, B. J. Lester, Y. Zhang, Y. Y. Gao, J. Freeze, V. S. Batista, P. H. Vaccaro, I. L. Chuang, L. Frunzio, L. Jiang, S. M. Girvin, and R. J. Schoelkopf, Efficient Multiphoton Sampling of Molecular Vibronic Spectra on a Superconducting Bosonic Processor, Phys. Rev. X 10, 021060 (2020).
- [9] T. R. Nelson, A. J. White, J. A. Bjorgaard, A. E. Sifain, Y. Zhang, B. Nebgen, S. Fernandez-Alberti, D. Mozyrsky, A. E. Roitberg, and S. Tretiak, Non-Adiabatic Excited-State Molecular Dynamics: Theory and Applications for Modeling Photophysics in Extended Molecular Materials, Chem. Rev. 120, 2215 (2020).
- [10] P. J. Ollitrault, G. Mazzola, and I. Tavernelli, *Nonadiabatic Molecular Quantum Dynamics with Quantum Computers*, Phys. Rev. Lett. **125**, 260511 (2020).
- [11] F. Schlawin, M. Gessner, A. Buchleitner, T. Schätz, and S. S. Skourtis, Continuously Parametrized Quantum Simulation of Molecular Electron-Transfer Reactions, PRX Quantum 2, 010314 (2021).
- [12] R. J. MacDonell, C. E. Dickerson, C. J. T. Birch, A. Kumar, C. L. Edmunds, M. J. Biercuk, C. Hempel, and I. Kassal, *Analog Quantum Simulation of Chemical Dynamics*, Chem. Sci. 12, 9794 (2021).
- [13] F. M. Gambetta, C. Zhang, M. Hennrich, I. Lesanovsky, and W. Li, Exploring the Many-Body Dynamics Near a Conical

- Intersection with Trapped Rydberg Ions, Phys. Rev. Lett. 126, 233404 (2021).
- [14] S. Chakram, A. E. Oriani, R. K. Naik, A. V. Dixit, K. He, A. Agrawal, H. Kwon, and D. I. Schuster, Seamless High-Q Microwave Cavities for Multimode Circuit Quantum Electrodynamics, Phys. Rev. Lett. 127, 107701 (2021).
- [15] S. Chakram, K. He, A. V. Dixit, A. E. Oriani, R. K. Naik, N. Leung, H. Kwon, W.-L. Ma, L. Jiang, and D. I. Schuster, *Multimode Photon Blockade*, Nat. Phys. 18, 879 (2022).
- [16] P. Bertet, A. Auffeves, P. Maioli, S. Osnaghi, T. Meunier, M. Brune, J. M. Raimond, and S. Haroche, *Direct Measure-ment of the Wigner Function of a One-Photon Fock State in a Cavity*, Phys. Rev. Lett. 89, 200402 (2002).
- [17] J. C. Tully, *Perspective: Nonadiabatic Dynamics Theory*, J. Chem. Phys. **137**, 22A301 (2012).
- [18] D. R. Yarkony, *Nonadiabatic Quantum Chemistry: Past, Present, and Future*, Chem. Rev. **112**, 481 (2012).
- [19] B. F. Curchod and T. J. Martínez, Ab Initio Nonadiabatic Quantum Molecular Dynamics, Chem. Rev. 118, 3305 (2018).
- [20] H. Köuppel, W. Domcke, and L. S. Cederbaum, Multimode Molecular Dynamics Beyond the Born-Oppenheimer Approximation, Advances in Chemical Physics Vol. 57 (Interscience Publishers, New York, 1984), pp. 59–246.
- [21] F. T. Smith, Diabatic and Adiabatic Representations for Atomic Collision Problems, Phys. Rev. 179, 111 (1969).
- [22] R. Schneider and W. Domcke, S1-S2 Conical Intersection and Ultrafast S2 → S1 Internal Conversion in Pyrazine, Chem. Phys. Lett. **150**, 235 (1988).
- [23] L. Seidner, G. Stock, A. L. Sobolewski, and W. Domcke, *Ab Initio Characterization of the S1–S2 Conical Intersection in Pyrazine and Calculation of Spectra*, J. Chem. Phys. **96**, 5298 (1992).
- [24] F. Aleotti, D. Aranda, M. Yaghoubi Jouybari, M. Garavelli, A. Nenov, and F. Santoro, Parameterization of a Linear Vibronic Coupling Model with Multiconfigurational Electronic Structure Methods to Study the Quantum Dynamics of Photoexcited Pyrene, J. Chem. Phys. 154, 104106 (2021).
- [25] A. Kühl and W. Domcke, Multilevel Redfield Description of the Dissipative Dynamics at Conical Intersections, J. Chem. Phys. 116, 263 (2002).
- [26] H.-G. Duan and M. Thorwart, *Quantum Mechanical Wave Packet Dynamics at a Conical Intersection with Strong Vibrational Dissipation*, J. Phys. Chem. Lett. 7, 382 (2016).
- [27] A. J. Schile and D. T. Limmer, Simulating Conical Intersection Dynamics in the Condensed Phase with Hybrid Quantum Master Equations, J. Chem. Phys. 151, 014106 (2019).
- [28] U. Manthe and H. Köppel, *Dynamics on Potential Energy Surfaces with a Conical Intersection: Adiabatic, Intermediate, and Diabatic Behavior*, J. Chem. Phys. **93**, 1658 (1990).
- [29] E. Teller, *The Crossing of Potential Surfaces*, J. Phys. Chem. **41**, 109 (1937).
- [30] W. Domcke and D. R. Yarkony, *Role of Conical Intersections in Molecular Spectroscopy and Photoinduced Chemical Dynamics*, Annu. Rev. Phys. Chem. **63**, 325 (2012).
- [31] C. Axline, M. Reagor, R. Heeres, P. Reinhold, C. Wang, K. Shain, W. Pfaff, Y. Chu, L. Frunzio, and R. J. Schoelkopf, An Architecture for Integrating Planar and 3D cQED Devices, Appl. Phys. Lett. 109, 042601 (2016).
- [32] J. Koch, T. M. Yu, J. Gambetta, A. A. Houck, D. I. Schuster, J. Majer, A. Blais, M. H. Devoret, S. M. Girvin, and

- R. J. Schoelkopf, *Charge-Insensitive Qubit Design Derived from the Cooper Pair Box*, Phys. Rev. A **76**, 042319 (2007).
- [33] S. Hacohen-Gourgy, L. S. Martin, E. Flurin, V. V. Ramasesh, K. B. Whaley, and I. Siddiqi, *Quantum Dynamics of Simultaneously Measured Non-Commuting Observables*, Nature (London) **538**, 491 (2016).
- [34] S. Gustavsson, J. Bylander, F. Yan, P. Forn-Díaz, V. Bolkhovsky, D. Braje, G. Fitch, K. Harrabi, D. Lennon, J. Miloshi et al., Driven Dynamics and Rotary Echo of a Qubit Tunably Coupled to a Harmonic Oscillator, Phys. Rev. Lett. 108, 170503 (2012).
- [35] D. Schuster, A. A. Houck, J. Schreier, A. Wallraff, J. Gambetta, A. Blais, L. Frunzio, J. Majer, B. Johnson, M. Devoret et al., Resolving Photon Number States in a Superconducting Circuit, Nature (London) 445, 515 (2007).
- [36] N. Didier, J. Bourassa, and A. Blais, Fast Quantum Nondemolition Readout by Parametric Modulation of Longitudinal Qubit-Oscillator Interaction, Phys. Rev. Lett. 115, 203601 (2015).
- [37] S. Touzard, A. Kou, N. E. Frattini, V. V. Sivak, S. Puri, A. Grimm, L. Frunzio, S. Shankar, and M. H. Devoret, *Gated Conditional Displacement Readout of Superconducting Qubits*, Phys. Rev. Lett. **122**, 080502 (2019).
- [38] J. C. Tully, Molecular Dynamics with Electronic Transitions, J. Chem. Phys. 93, 1061 (1990).
- [39] J. E. Subotnik, A. Jain, B. Landry, A. Petit, W. Ouyang, and N. Bellonzi, *Understanding the Surface Hopping View of Electronic Transitions and Decoherence*, Annu. Rev. Phys. Chem. 67, 387 (2016).
- [40] K. S. Chou, J. Z. Blumoff, C. S. Wang, P. C. Reinhold, C. J. Axline, Y. Y. Gao, L. Frunzio, M. Devoret, L. Jiang, and R. Schoelkopf, *Deterministic Teleportation of a Quantum Gate between Two Logical Qubits*, Nature (London) **561**, 368 (2018).
- [41] J. Gambetta, A. Blais, M. Boissonneault, A. A. Houck, D. I. Schuster, and S. M. Girvin, *Quantum Trajectory Approach to Circuit QED: Quantum Jumps and the Zeno Effect*, Phys. Rev. A 77, 012112 (2008).
- [42] N. Frattini, U. Vool, S. Shankar, A. Narla, K. Sliwa, and M. Devoret, *3-Wave Mixing Josephson Dipole Element*, Appl. Phys. Lett. **110**, 222603 (2017).
- [43] S. O. Mundhada, A. Grimm, J. Venkatraman, Z. K. Minev, S. Touzard, N. E. Frattini, V. V. Sivak, K. Sliwa, P. Reinhold, S. Shankar et al., Experimental Implementation of a Raman-Assisted Eight-Wave Mixing Process, Phys. Rev. Appl. 12, 054051 (2019).
- [44] J. Larson, Jahn-Teller Systems from a Cavity QED Perspective, Phys. Rev. A 78, 033833 (2008).
- [45] J. Larson, Analog of the Spin-Orbit-Induced Anomalous Hall Effect with Quantized Radiation, Phys. Rev. A 81, 051803(R) (2010).
- [46] D. Polli, P. Altoè, O. Weingart, K. M. Spillane, C. Manzoni, D. Brida, G. Tomasello, G. Orlandi, P. Kukura, R. A. Mathies, M. Garavelli, and G. Cerullo, *Conical Intersection Dynamics of the Primary Photoisomerization Event in Vision*, Nature (London) 467, 440 (2010).
- [47] A. Grimm, N.E. Frattini, S. Puri, S.O. Mundhada, S. Touzard, M. Mirrahimi, S.M. Girvin, S. Shankar, and M. H. Devoret, *Stabilization and Operation of a Kerr-Cat Qubit*, Nature (London) **584**, 205 (2020).

- [48] L. D. Burkhart, J. D. Teoh, Y. Zhang, C. J. Axline, L. Frunzio, M. H. Devoret, L. Jiang, S. M. Girvin, and R. J. Schoelkopf, Error-Detected State Transfer and Entanglement in a Superconducting Quantum Network, PRX Quantum 2, 030321 (2021).
- [49] J. C. Owens, M. G. Panetta, B. Saxberg, G. Roberts, S. Chakram, R. Ma, A. Vrajitoarea, J. Simon, and D. I. Schuster, *Chiral Cavity Quantum Electrodynamics*, Nat. Phys. **18**, 1048 (2022).
- [50] W. Domcke, D. Yarkony, and H. Köppel, *Conical Intersections: Electronic Structure, Dynamics & Spectroscopy*, Vol. 15 (World Scientific, Singapore, 2004).
- [51] Y. Lu, S. Chakram, N. Leung, N. Earnest, R. K. Naik, Z. Huang, P. Groszkowski, E. Kapit, J. Koch, and D. I. Schuster, *Universal Stabilization of a Parametrically Coupled Qubit*, Phys. Rev. Lett. **119**, 150502 (2017).
- [52] K. W. Murch, U. Vool, D. Zhou, S. J. Weber, S. M. Girvin, and I. Siddiqi, *Cavity-Assisted Quantum Bath Engineering*, Phys. Rev. Lett. 109, 183602 (2012).
- [53] W. Pfaff, C. J. Axline, L. D. Burkhart, U. Vool, P. Reinhold, L. Frunzio, L. Jiang, M. H. Devoret, and R. J. Schoelkopf, Controlled Release of Multiphoton Quantum States from a Microwave Cavity Memory, Nat. Phys. 13, 882 (2017).